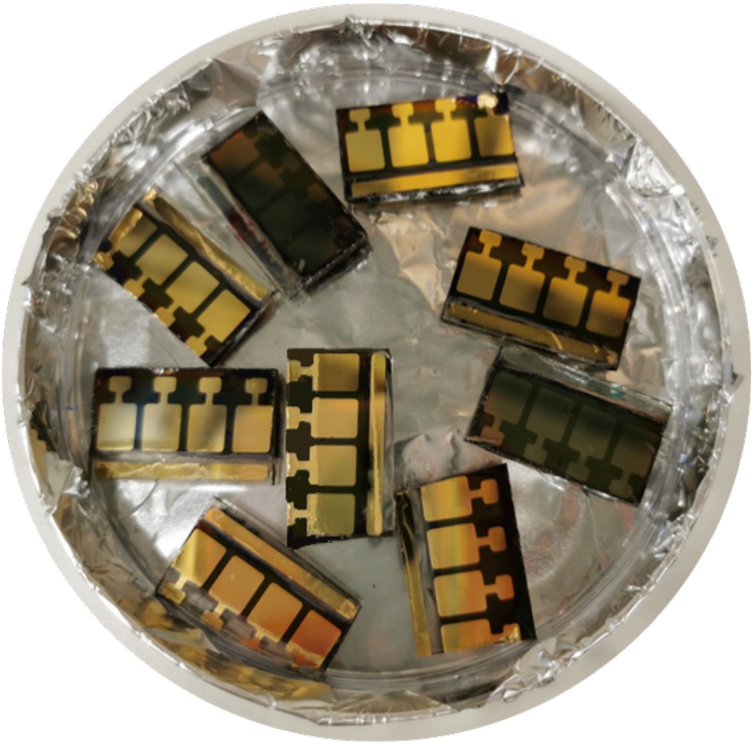

Increasing the efficiency of perovskite solar cells by interface engineering

Initial characterisations of the effect of adding an ammonium salt to the SnO_2 electron transport layer

Master's thesis in engineering physics

VICTORIA BERLING

DEPARTMENT OF CHEMISTRY AND CHEMICAL ENGINEERING
CHALMERS UNIVERSITY OF TECHNOLOGY
Gothenburg, Sweden 2022

MASTER’S THESIS 2022

Increasing the efficiency of perovskite solar cells by interface engineering

Initial characterisations of the effect of adding an ammonium salt to the SnO_2 electron transport layer

VICTORIA BERLING

CHALMERS
UNIVERSITY OF TECHNOLOGY

Department of Chemisty and Chemical engineering
CHALMERS UNIVERSITY OF TECHNOLOGY
Gothenburg, Sweden 2022

Increasing the efficiency of perovskite solar cells by interface engineering
Initial characterisations of the effect of adding an ammonium salt to the SnO_2 electron transport layer
VICTORIA BERLING

Supervisor: Gerrit Boschloo, Uppsala Univeristy
Advisor: Bowen Yang, Uppsala University
Examiner: Maria Abrahamsson, Department och Chemistry and Chemical engineering, Physical Chemistry

Master's Thesis 2022
Department of Chemistry and Chemical engineering
Chalmers University of Technology and University of Gothenburg
SE-412 96 Gothenburg
Telephone +46 31 772 1000

Cover: Perovskite solar cells manufactured and ready to be examined placed in a petridish covered in aluminium foil.

Typeset in LaTeX
Gothenburg, Sweden 2022

Abstract

Perovskite solar cells (PSCs) are continuously evolving and showing great potential with a rapidly increasing power conversion efficiency (PCE) over the last few years. To achieve even higher PCE, interface engineering of the electron transport layer (ETL) in the PSC is a promising approach. A novel ammonium salt is evaluated for $MAPbI_3$ based PSCs. The cells are manufactured in ambient condition, with the ammonium salt either as an interfacial treatment or as an additive in the bulk of the ETL which consists of tin oxide (SnO_2). The interfacial treatment does not seem to have a significant effect on the PCE, but the cells manufactured with the bulk additive show promising results with the highest efficiency being 22.8%. To gain insight on the reason behind the observed improvement in efficiency, some characteristics of the ETL and perovskite (PSK) films are investigated. The analysis indicates that the particle size of the SnO_2 increases with the amount of additive, as well as the surface roughness of the SnO_2 film. Furthermore, it is observed that the additive in lower concentration slightly enhances the electron extraction capability of the SnO_2 film, and in high concentration seems to slightly inhibit the electron transport by increasing the blocking properties of the SnO_2 film. The trends observed are highly preliminary and to confirm the results and increase the understanding of the properties of the modified ETL, further studies are required.

Keywords: Ambient manufacturing, Electron transport layer, interface engineering, Perovskite solar cell, tin oxide, SnO_2.

Sammanfattning

Solceller baserade på perovskit (PSC) är under ständig utveckling och visar stor potential med snabbt ökande uppnådda effektiviteter under de senaste åren. För att uppnå ännu högre effektivitet, har bearbetning av gränsytan för elektron transport lagret (ETL) visat sig vara en effektiv metod. Ett ammoniumbasterat salt evalueras i denna studie för en solcell baserad på perovskitmaterialet $MAPbI_3$. Solcellerna produceras i rumstemperatur under normala förhållanden med ammonium saltet tillsatt antingen som en behandling på gränsytan eller som en tillsats i bulken av ETL som består av tennoxid (SnO_2). Behandlingen av gränsytan verkar inte ge någon större effekt på solcellernas effektivitet, medan solcellerna med ammoniumsaltet som tillsats visar lovande resultat med den högsta effektiviteten 22.8%. För att få större insikt av de bakomliggande orsakerna till den observerade förbättringen i effektivitet, undersöks några egenskaper hos ETL och perovskit (PSK) filmerna. Analyserna indikerar att partikelstorleken av SnO_2 ökar med mängden tillsatt ammoniumsalt, liksom ytans strävhet hos SnO_2 filmen. Vidare observeras det att vid en lägre koncentration av tillsatt ammoniumsalt ökar SnO_2 filmes förmåga att extrahera elektroner marginellt, medan en högre koncentration verkar hämmande på elektrontransporten i SnO_2 filmen genom att öka blockeringsförmågan i filmen till en viss grad. De observerade trenderna är preliminära, så för att verifiera resultaten och få större insikt om egenskaperna hos de modifierade ETL krävs fortsatta studier.

Nyckelord: Berabetning av gräsnyta, Elektron transport lager, Solcell baserad på perovskit, Tillverkning under normala förhållanden, tennoxid, SnO_2

Acknowledgements

During my work with this thesis I have received great support from many wonderful persons, and I will take this opportunity to express my gratitude.

I would first of all like to thank Prof. Gerrit Boschloo for the opportunity to carry my thesis through in the Boschloo Group at Uppsala University and for his guidance. I would also like to thank my advisor Bowen Yang for the immense support, patience and fruitful discussions as well as teaching me all I know about manufacturing solar cells together with Jiajia Suo. Without them this project would not have been possible.

Furthermore I would like to thank my amazing colleagues Aneta Andruszkiewicz, Anuja Vijayan, Catherine Johnson, Erik Johansson, Fiona Treber, Fuxiang Ji, Lars Flauger, Malin Johansson and Yawen Liu for great office and lab company as well as for advice and rewarding discussions.

Finally I would also like to give an immense thank you to my family and friends who have been supporting me throughout this period, I am very grateful for you all.

Victoria Berling, Gothenburg, August 2022

Contents

1 Introduction

The greenhouse effect is a natural and vital phenomena, being the reason why our planet is suitable for life as we know it [1]. The greenhouse effect is caused by greenhouse gases (GHGs) such as carbon dioxide (CO_2) and methane, which absorb and reradiate infrared light leading to heat being kept within the atmosphere of the earth. Since the industrial revolution, the concentration of GHGs in the atmosphere has reached record high levels, leading to an enhanced greenhouse effect and in turn to global warming [1, 2]. As the global mean temperature rises, the severe effects of the global warming are becoming more predominant, and many potential consequences are still challenging to foresee [1, 3].

At the same time as the global temperature is increasing, so is the global population [4]. Moreover the global population is becoming more urbanised, leading to higher energy demands worldwide. In 2021 the worldwide energy demand saw its largest annual increase ever, boosted by a rapid economic growth after the pandemic and a colder than average winter due to more extreme weather conditions in 2020 [5]. The energy demand was to the greatest extent met by coal-fired generated electricity, and the CO_2 emissions in total from the electricity generating sector rose to record high levels. In the beginning of 2022 more complexity was added to the quest of energy supply as Russia invaded Ukraine, causing an urge for Europe to reduce the reliance of Russian gas and coal [6]. As a measure to take action the European Union developed and released a plan called REPowerEU, with the goal to end the EU's dependence on fossil fuels from Russia and to accelerate the installation of renewable energy sources [7].

The above mentioned aspects are of great importance when discussing energy sources and energy supply, and the topic has been extensively depicted in the Global Sustainability Goals [8]. One main point is that energy stands for 73 % of the human caused GHGs released yearly, and is thereby the main contributor to the enhanced greenhouse effect. In 2015 the Paris agreement was signed and is today being followed by 193 parties, who strive toward a net-zero emission of GHGs to keep the global temperature increase below 1.5 $\deg$ C [9]. A key factor to achieve the goals of the Paris agreement and thereby limit the climate change already making its presence felt, is renewable energy [1].

Through renewable energies it is possible to tackle both the climate crisis, and an increased energy demand at the same time [10]. Among the renewable energies produced from sunlight, wind and water, solar energy is the most promising [11]. The solar energy is the most abundant energy source: The amount of energy that reaches the earth in terms of electromagnetic radiation from the sun is 10 000 times greater than the energy consumption of the globe at any given time. To capture this solar energy, solar panels (also known as solar cells), have been developed and implemented on the market, and development of new models of solar cells is still a hot research topic [10, 12].

1.1 Solar cells and a classical PV model

The power that reaches the earth on a clear day is approximately 1 kW/m^2 at sea level, rendering the sun an extremely powerful energy source [13]. Solar panels have been developed to collect this energy and turn it into electricity. This was done for the first time in 1883 by Charles Fritts using thin metal films and selenium. About two decades later, in 1905, Albert Einstein clarified the theoretical fundamentals of the photoelectric effect, discovered by Edmond Becquerel in 1839, shedding light on why the photovoltaic panel worked. Today a wide variety of photovoltaic cells are investigated, all with the goal to transform as much sunlight as possible into electricity. The theoretical maximum efficiency for these cells is given by the Shockley-Queisser limit as 33.7% [14], and today cells deviating less than ten percentage units from this limit can be produced [15]. The different kinds of solar cells have different designs, but their working principle can be generalised according to a classical PV model with a silicon (Si) solar cell as an example.

The classical PV model based on a Si solar cell describes a silicon p-n junction with metal electrodes, or contacts, at the top and bottom [13]. In the centre of the p-n junction the active area of the cell, also known as the depletion region, is formed. A p-n-junction with the depletion region is illustrated in figure 1.1, where the red circles represent holes and the blue circles represent electrons. A p-n-junction is formed from n- and p-type silicon as illustrated in figure 1.1. The p-type Si is formed by Si doped by boron (B) atoms. The B atoms only have three valence electrons, therefore the p-type Si has an excess of loose holes. The n-type Si is doped with phosphor (P) atoms, which have five valence electrons. Therefore the n-type Si has an excess of loosely bound electrons. When these two materials are in joint, the excess electrons in the n-type Si will diffuse towards the p-type side, and the holes in the p-type will diffuse towards the n-type side. As the carriers accumulate on each side a net charge is created, which will prevent further diffusion as it grows larger. The area with the net charge is the formed depletion region.

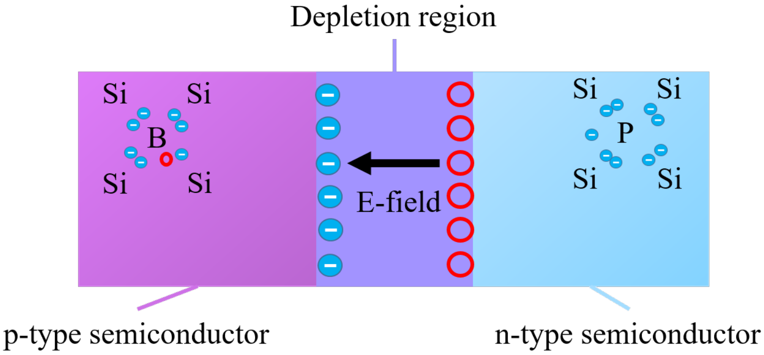

Figure 1.1: *Illustration of a Si p-n-junction and the depletion region.*

The depletion region has an internal electric field due to the net charge, such that when a photon strikes the semiconductor material and creates a free electron-hole pair as the electron is excited to the conduction band (CB), the charges are immediately separated. This separation of charges results in the photocurrent creating the electricity output. In Si solar cells the p-n junction is created by putting together n- and p-doped Si and thus forming the p-n junction and the depletion region [13].

1.2 Solar cells and their current status

Today, solar cells with silicon as the semiconductor material dominate the market with efficiencies of about 22-25% [16, 13]. The widespread use of Si in SCs is thanks to the bandgap of the material, which is about 1.17 eV, and because high quality silicon is easily accessed through semiconductor Si wafer production, for example for microchips [17]. Therefore Si solar cells based on wafers, which are often referred to as part of the so called 1:st generation solar cells, were convenient to produce. However, the production of Si wafers requires expensive and energy consuming manufacturing, as well as a high installation cost of the solar cell modules [16, 13, 17]. The high installation cost is partly due to the fact that the Si solar cells require a few 100 μm thick film of

Si to achieve high efficiencies, since Si has an indirect bandgap which implies that the absorption coefficient is relatively low [13]. This results in heavy modules and a higher material cost. These areas of possible improvement have led to a large interest in exploring alternative materials to Si wafers [13, 17].

As a consequence both second and third generation solar cells have been developed, where the first mentioned mainly consisting of thin film SCs and the last mentioned of SCs consisting of novel combinations and designs of materials, such as perovskite (PSK) [16, 13, 17]. With the thin films, semiconductor materials are deposited in layers on a scale of a few μm onto substrates which can be made of glass or plastic [13, 17]. The materials used have a direct bandgap which makes it possible to have a thin film, but still reach relatively high efficiencies. The production of the thin film cells is less energy requiring and less expensive since the amount of material required to produce a device is low. The possibility of making flexible substrates also opened up for new applications, such as wearable SCs.

The third generation solar cells are also produced as thin films, but using novel combinations and designs of materials, and are no longer relying on the typical semiconductor pn-junction as was the case with the first two previous generations [13, 17]. Among the third generation SCs the dye sensitized solar cells (DSSCs), quantum dot solar cells and perovskite solar cells (PSCs) are found. The DSSCs are based on a dye that absorbs sunlight just like chlorophyll does in plants. The absorbing molecule in the quantum dot solar cell is a semiconducting particle obeying quantum mechanical laws, and for the PSCs the absorbing material is perovskite. One of the advantages of the PSK material is that the bandgap can be tuned. This means that the bandgap can be optimised for light absorption of certain wavelengths and thereby increase the efficiency of the cell. Out of the dye-sensitized, quantum dot and perovskite solar cells, the perovskite solar cells have so far shown the greatest efficiencies, and they are therefore of great interest for further research [18].

An extensive overview of the status efficiency-wise for different kinds of SCs is provided by the National Renewable Energy Laboratory (NREL) [15] and can be seen in figure 1.2.

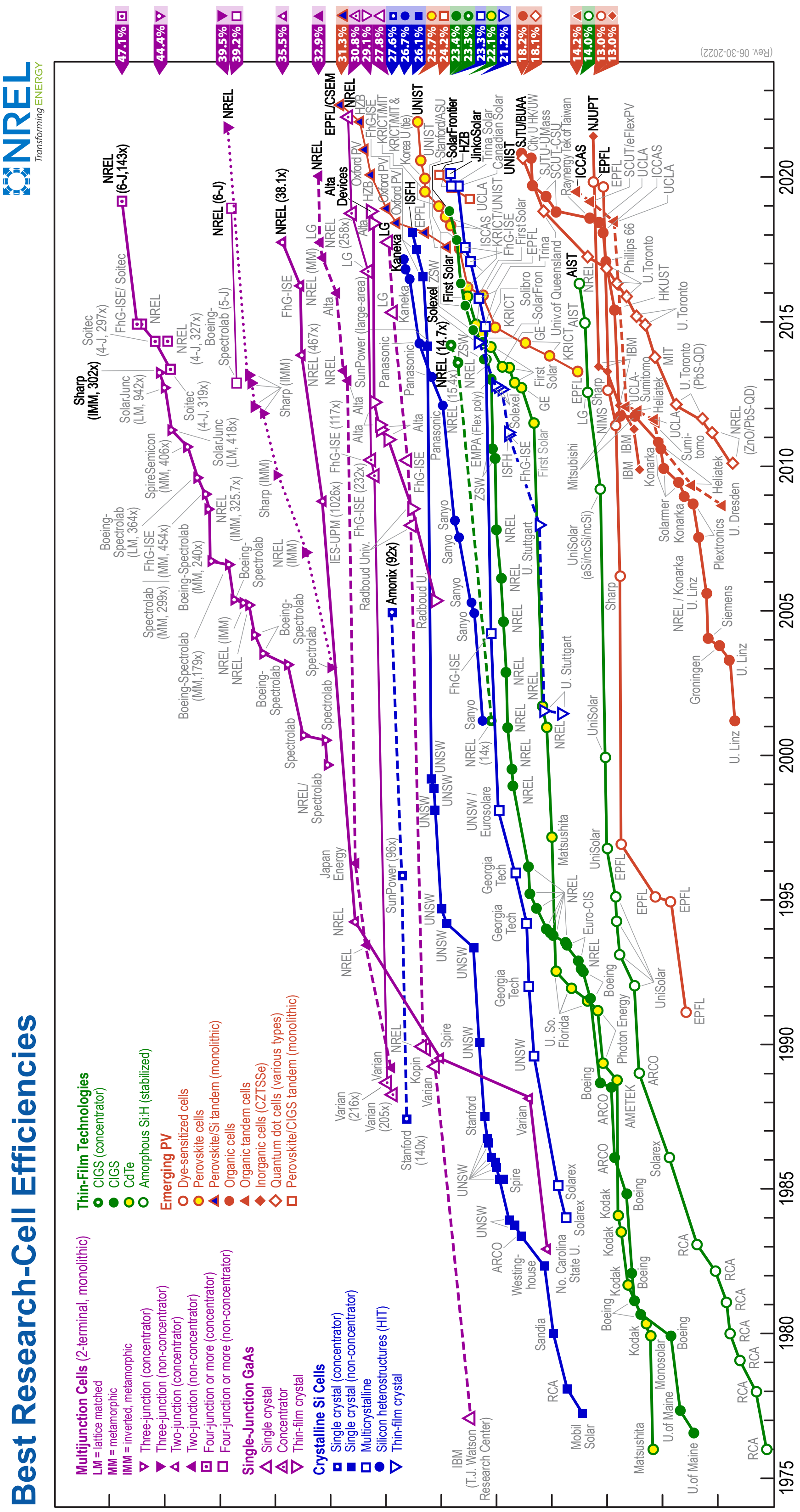

Figure 1.2: *Overview of best efficiencies for each kind of solar cells, figure provided by NREL [15]*

As can be seen in figure 1.2, perovskite solar cells have developed from efficiencies of about 12% in 2013 to the current record of 25.7% in 2022, which is one of the most promising developments observed in the chart [15]. PSK is a low cost material, and the PSCs can be manufactured in a low cost process, making the PSCs interesting as a candidate for production of SCs on a larger scale [16]. However, further research must be conducted to find more stable PSCs with high efficiency before PSCs can released onto the market. To achieve this, a broad understanding of the function of PSK, the PSCs and possible ways to improve the cells is necessary.

2 Background of perovskite solar cells

2.1 The perovskite material

Perovskite is a mineral originally found in the Ural Mountains in Russia by Gustav Rose in 1939 [16]. The mineral was named after the mineralogist Count Lev Alekseevich Perovski who carried the research on the mineral. The mineral in the Ural mountains had the chemical structure $CaTiO_3$. It is based on the structure of this mineral that the perovskite for solar cells is made. The PSK used for solar cells has a crystal structure with the general formula ABX_3. The components of the crystal structure can be varied to achieve different properties, such as varying the bandgap. The general crystal structure of PSK can be seen in figure 2.1a, where the octahedral structure of the PSK through BX_6 is visible.

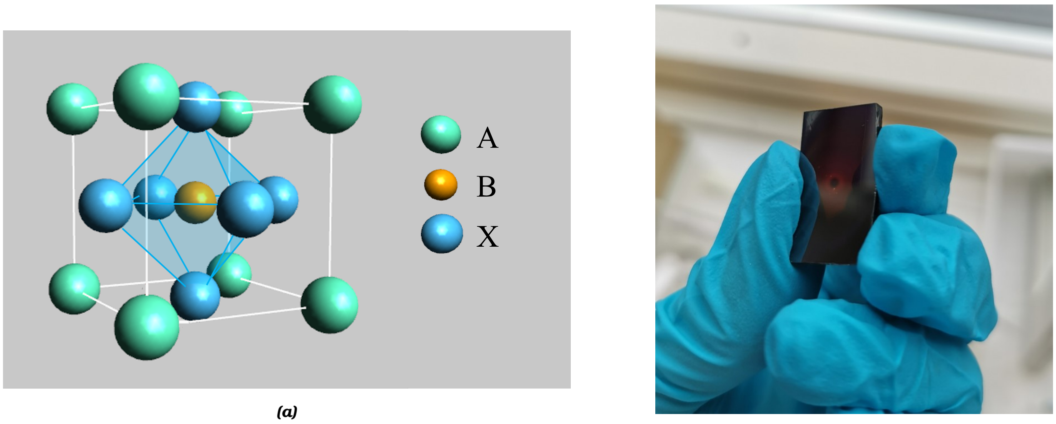

(a)

(b)

Figure 2.1: *Organic-inorganic PSC.* ***(a)*** *The general crystal structure of perovskite with the general formula* ABX_3*.* ***(b)*** *A deposited PSK film onto a glass substrate. The circular shape in the middle is a spin coating defect.*

One extraordinary property of perovskites which is highly useful in the making of PSC is that the bandgap of the PSK can be tuned [17]. This means that depending on the composition of the crystal, the bandgap of PSK can be altered to find a value between 1.5-3 eV. By designing the bandgap value in a clever way, the absorption and transport of electrons in a solar cell can improve, leading to a higher efficiency cell. One important group of perovskites are the so called organic-inorganic perovskites. For such perovskites A is an organic monovalent cation, e.g. Methylammonium (MA, $CH_3NH_3^+$) or formamidinium (FA, $CH(NH_2)_2^+$), B is a divalent cation such as Pb^{2+} or Sn^{2+}, and X is a halogen anion such as I^- or Br^- [16, 19].

For PSCs one of the most common perovskite is the organic-inorganic perovskite methylammonium lead trihalide $MAPbI_3$ [16]. In figure 2.1b a $MAPbI_3$ film deposited onto a glass substrate can be seen. The film is dark brown/black in colour with an even surface and slightly transparent. The circular shape in the middle of the film is a defect from the manufacturing process. The $MAPbI_3$ used in the project has a direct bandgap of approximately 1.55 eV [20] which is a close to optimal bandgap for absorption of light [17]. Another favourable property of the PSK is the low processing temperature needed in the manufacturing process ($< 150°$ C). At the time of writing this report, the record efficiency for a $MAPbI_3$ PSC is between 22%-23% [21].

A downside with the PSK material is its sensitivity of humidity and its tendency to degrade [22, 23]. PSK is very sensitive to moisture since the H_2O molecule causes hydrogen bonds in the PSK to break as the molecules make their way into the PSK lattice [24]. The water molecule will in the case of $MAPbI_3$ interact with the MA cation, such that it is no longer strongly bonded to the lattice. The octahedral structure will then get destabilised and the PSK structure will degrade. Furthermore, as PSK is illuminated ion migration can be facilitated, hence causing degradation of the crystal structure [22]. To further find suitable materials to help improve the efficiency and stability of the cell, research within the field of PSC is of utmost importance [22, 23].

Because of the sensitivity to moisture, PSK solar cells are most often fabricated on a small scale in a dry environment using moisture free gloveboxes [25]. This type of fabrication increases the manufacturing cost, and limits the possibility of up-scaling to an industrial level. However, it has been shown that it is possible to achieve high efficiency solar cells in ambient conditions using $MAPbI_3$, with cells reaching efficiencies of around 19% [26].

2.2 Operational principles of a perovskite solar cell

The energetic bandgap E_g of the absorbing material is of great importance to obtain a high performing SC, which is why the tuneability of the PSK is a great advantage of the material [17, 27]. The importance of the bandgap is due to its effect on the probability of excitation of the electrons. For the electrons in the absorbing layer to be excited, the incoming photon must have energy higher or equal to E_g. This means that a SC with one absorbing material, such as PSK, cannot absorb the whole spectrum emitted by the sun, which consists of a vast range of wavelengths [17, 28]. Instead photons with energy $h\mu < E_g$ will not lead to any excitation of electrons, so these wavelengths are referred to as spectral losses [29]. Photons with much larger energy than the bandgap $h\mu >> E_g$ will excite electrons and contribute to the current, but their excess energy will lead to thermal losses. In other words there is a range of energies for which the photons have equal or larger energy than the bandgap $h\mu \geq E_g$, and hence exciting electrons and generating current with good efficiency.

The photovoltaic cell can therefore only use sunlight with energy higher than E_g to convert sunlight to energy [29]. But converting more photons does not automatically imply having a better photovoltaic cell, because E_g determines the maximum voltage output of the cell: The larger E_g, the higher the output voltage. But as mentioned above, a higher E_g means that a smaller amount of the sunlight can contribute to exciting electrons. There is therefore a trade-off between a large E_g to obtain higher voltage, and a small E_g to absorb more photons. From this trade-off, Shockley and Quiesser calculated the theoretical maximum efficiency for a solar cell containing one absorbing material to be 33.7% for a bandgap of 1.4 eV [14]. As mentioned earlier, $MAPbI_3$ has a bandgap of 1.55 eV, which is close to the optimal value.

2.2.1 Structure of the cell

As described earlier using a classical PV model, the active area of a solar cell is formed in the depletion region of a p-n-junction by a semiconductor material [13]. In a PSK solar cells, the PSK is sandwiched between an n-type material, also known as the electron transport layer (ETL), and a p-type material, also known as the hole transport layer (HTL) [30]. Thereby the PSK is not doped as the Si in silicon solar cells, but the depletion region is rather created by adding materials at each side of the PSK. In this way, the depletion region will be formed in the PSK, and thus the free carriers created upon illumination will be separated due to the internal electric field. Often this separation and transport of charges is referred to as extraction of charges by the ETL and HTL. The layers are deposited onto conductive glass, which is glass most commonly covered either by fluorine doped tin oxide (FTO) or indium doped tin oxide (ITO). In this project conductive glass with FTO will be used. It is now clear that a PSC consists of five main layers: The metal contacts at the top and bottom of the cell, the ETL, the HTL, the FTO and the absorbing material which is the PSK. These layers and their properties are of high importance for the performance of the perovskite solar cells.

One common structure and function of a PSC is seen in figure 2.2 [29]. The contact electrode (CE) is commonly made out of a noble metal such as gold (Au), but ongoing research strives to find a more sustainable alternative in carbon materials such as graphite [31, 32]. A widely used HTL material is Spiro-MeOTAD (will be referred to as spiro) which forms a good contact with the PSK [33]. For the ETL, tin oxide (SnO_2) or titanium oxide (TiO_2) are commonly used materials. Typical thicknesses of the films are below 200 nm for ETL, HTL and FTO, a few hundred nm for PSK and below 100 nm for the CE [33].

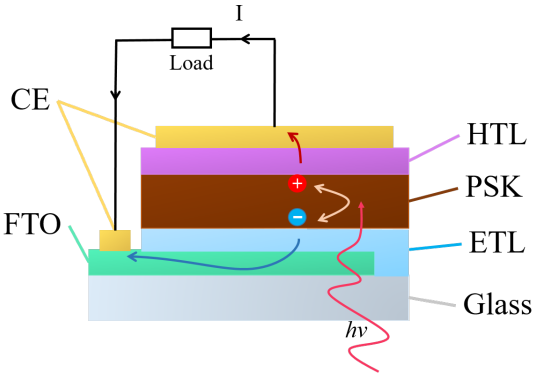

Figure 2.2: *General structure of the layers in a perovskite solar cell and its working principle.*

The layers should have a good surface coverage and have good contact for optimal performance [34]. One common defect in the films are so called pinholes, which are holes in the films in a size range of nm-μm and hence not visible to the eye. When pinholes occur in the PSK film, the HTL and ETL will be in contact through the pinholes which can lead to short circuit of the cell. It is therefore if high importance that the films are of good quality with a high surface coverage.

2.2.2 Function of the perovskite solar cell

In a PSC, the absorption of light in the PSK leads to generation of free charges, which are electrons (e^-) and holes (h^+), also commonly denominated as carriers, which is illustrated in figure 2.2 [20]. Another way to represent a PSC is through the energy levels of the layers. Such an illustration is seen in figure 2.3 where the E_g is the gap between the VB and CB level. When a photon with sufficient energy excites an electron to the conduction band a hole is left behind in the valence band as illustrated by process 1 in the figure. A current is created when the electrons and holes are injected into the electron transport layer (ETL) and hole transport layer (HTL) respectively as illustrated by process 2, and then extracted into an outer circuit through process 3.

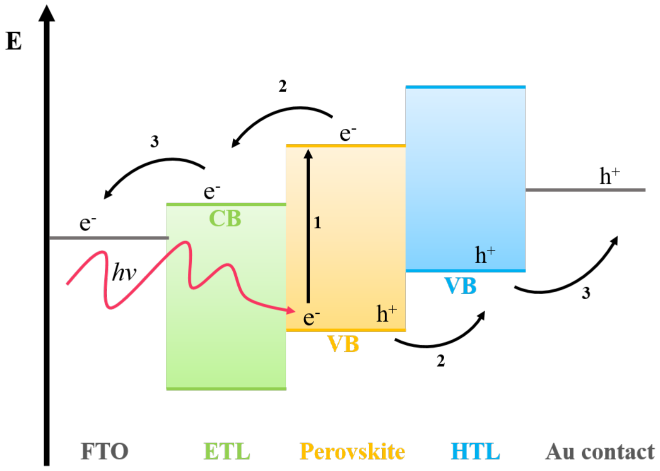

Figure 2.3: *Energy levels of the fluorine doped tin oxide (FTO), electron transport layer (ETL), the perovskite, the hole transport layer (HTL) and the gold (Au) metal contact in a PSC.*

For the injection of carriers to occur, the energy band alignment of the ETL, perovskite and HTL should preferably have the general shape illustrated in figure 2.3 [20]. That is, the CB and VB of the ETL are both lower than, and the CB and VB of the HTL are both higher than, the CB and VB of the perovskite. In this way, the excited electrons will be injected into the CB of the ETL, which has lower energy than the CB of the perovskite. The electrons will then be injected further into the layer of fluorine doped tin oxide (FTO) from which they are led to an outer circuit. The holes will be injected in the opposite direction, which is into the VB of the HTL, and then further to the metal contact and from there to the outer circuit. It is through this injection and extraction of electrons and holes that a current is produced from a solar cell. The more photons that are absorbed and generating carriers which contribute to the current, the higher the efficiency of the solar cell.

One important point to take notice of, is that not all generated free carriers will contribute to the current [20]. This is due to recombination of the carriers which can occur in different ways. For example, if an electron is generated close to the perovskite/HTL interface, it will have to diffuse through the perovskite layer to reach the ETL. The opposite is true for holes generated near the ETL/perovskite interface. It is then possible that the electron will encounter a hole and recombine, hence not contributing to the current. Recombination that occurs through such a process is often referred to as bulk recombination. Another possible mechanism is recombination at the interfaces, which can be due to interfacial defects in the materials or bad energy level alignment, and is hence referred to as interfacial recombination [35]. The interfacial recombination is the dominating recombination process in the PSC, and hence the most important recombination process to be tackled to reach higher efficiency PSCs [36, 35]. This can be done for example by improving the properties of the ETL.

2.3 The importance of the electron transport layer

The electron transport layer has a crucial function in the SC as it decreases the potential barrier for the electrons to transfer to the CE, while it blocks the holes, thus functioning as a charge selective layer [37]. To properly function in the SC and extract electrons with high efficiency the ETL material needs to meet three important requirements. First of all it must have good transparency to let light through such that the photons can be absorbed by the PSK. Secondly the E_g must be well aligned with the PSK to extract electrons and block holes as described earlier. And lastly the material must have high electron mobility to avoid charge accumulation in the ETL. Some commonly used materials that meet these requirements are some metal oxide semiconductors such as tin dioxide (SnO_2) and titanium dioxide (TiO_2).

A common and classic ETL material is the TiO_2 which has a high electrical conductivity [37]. In SC with a mesoporous structure the TiO_2 has been widely used and showed good results [38]. However, the TiO_2 films need processing at very high temperatures (500°C), and for compact thin films which are used in the structure showed in figure 2.2 SnO_2 is preferred [38]. The SnO_2 film has a high electron mobility in the bulk, one order of magnitude larger than TiO_2 and is more stable under illumination. It has a bandgap of approximately 3.6 eV and is thus not blocking the photons meant to be absorbed by the PSK [39]. The SnO_2 films can be treated at 150°C and are hence easier and less energy consuming to fabricate [38]. Although the SnO_2 film has many good properties, there is still room for improvement [22, 40]. An ideal SnO_2 would be thin enough to avoid charge accumulation, and at the same time the defects and pinholes would be minimised [40]. Modifications that could improve these problems can be reached through interface engineering.

2.3.1 Interface engineering

To avoid recombination of the carriers at the interfaces of the materials in the PSC, research focusing on the interfaces is carried out to optimise the charge transport between the layers, and the field is commonly called interface engineering [22, 23]. To avoid recombination due to bad energy alignment for the bandgaps of the different layers, extra layers can be added at the interfaces to improve the energy band alignment. For example, a layer of a small organic molecule (adenine) was added at the PSK/HTL interface which resulted in a reduction of the energy offset between the PSK and HTL, and thereby the performance of the cell increased [41]. But interface engineering does not strictly imply addition of layers, it can also be done by altering an already present layer in the PSC structure to affect its properties [23]. One example of this is a treatment of the ETL that was done using NH_4F and which reduced the defect sites of the layer as well as tuning the energy level of the ETL. This both reduced recombination of charges due to reduced interfacial traps, and through better energy alignment [22, 42].

Interface engineering of the SnO_2 film can be done in a few different ways with different goals, and is a method that has been used to improve the properties of the ETL in the solar cell and thereby increase the cell performance [43]. Some examples of goals with the interface engineering are to modify the band energy of the SnO_2 to improve the electron injection and hole blocking, or to passivate the surface to avoid recombination, or to improve the contact between the absorbing layer and the ETL. The surface engineering can be done by different approaches. One approach is to add a material on top of the SnO_2 film, a so called interfacial layer, to modify its surface. Another approach is to add a material into the SnO_2 film, a so called bulk additive, to modify the film properties. The materials can be both organic and inorganic molecules, and a big number of different approaches have already been tried [43, 22].

One approach of interface engineering which has been showing good results is using ammonium salts in and on the SnO_2 [22, 44]. When added as an interfacial layer, the ammonium salts can generally passivate both positive and negative ionic defects through chemical bonding [22]. It is also possible that ammonium salts can reduce carrier recombination through their dielectric properties. However, for the ammonium salts to have these properties, it is crucial that it has suitable chemical groups for passivation, as well as not altering the PSK structure.

The main focus of the interface engineering with the ammonium salts has been on the HTL where it has shown promising results and capability to increase the efficiency of the cells [22]. But there has also been some progress on the ETL; One ammonium salt that has recently showed good effect on the ETL layer is ammonium formate ($HCOONH_4$) [45]. This is a volatile organic salt that was added into the SnO_2 bulk, and which helped increase the efficiency of the SC. A novel salt with the same functional groups as ammonium formate ($HCOO^-$-group and NH_3^--group) has been developed and is ready for testing as an interfacial treatment and bulk additive.

3 Aim

The aim of the project is to investigate how a novel ammonium salt at the ETL/PSK interface will affect the efficiency of a PSK solar cell. The ammonium salt will be investigated both as an interfacial layer, and as an additive in the ETL bulk.

3.1 Limitations

In the project, only one kind of perovskite will be considered, and that will be $MAPbI_3$. Other types of perovskites will not be considered, even though they can be common in PSCs. Furthermore only one type of HTL, namely spiro-OMeTAD, will be considered in the device. The ETL will consist of SnO_2, and will be the component on which the interface engineering is performed. The CE will be evaporated gold and the substrate will be glass coated with FTO. The PSCs will be manufactured in ambient condition. Furthermore, the focus of the project will not be on the ammonium salt itself, but rather on the SnO_2 film and its properties after interaction with the ammonium salt. The ammonium salt used is newly developed and has not, to the best of the author's knowledge, been investigated in a PSC previously. Details of the chemical structure and composition of the novel ammonium salt will not be given, since the salt is of interest for further investigations with the goal of future publication.

3.2 Specification of issue under investigation

To further specify the issues under investigation of the project, some questions which should be answered through the project are:

1. How can the ETL be modified with the novel ammonium salt to produce higher efficiency cells?
2. How is the solar cell efficiency affected by the ammonium salt?
3. How can the effect of the ammonium salt in the ETL be characterised?

4 Methods and characterisation for solar cells

Knowledge about the process of manufacturing a solar cell is of importance to this thesis. When making a solar cell in a laboratory some methods and techniques that are not considered general knowledge are used, and these will therefore be introduced in this chapter. Once the solar cell device has been manufactured it is characterised, and these methods will also be explained as well as some general benchmark values used to determine the performance of a solar cell.

4.1 Experimental methods

There are different methods to create the thin films desired in a PSC, and depending on the size of the fabricated cells different methods can be used [16, 46]. For small scale fabrication of cells, spin coating of the films is a widely used method yielding uniform films. Before the films can be deposited onto the substrate, the substrates are cleaned using a sonicator and a UV-Ozone treatment. These methods will be further explained in this chapter.

4.1.1 Spin coating

The basic principle of spin coating is depositing a solution onto a substrate, then rotating the substrate at a high speed such that the solution spreads, and then letting the solution evaporate to create a solid thin film [47]. Even though the principle is simple, a lot of different settings and parameters can be tuned to modify the thickness and properties of the film.

The first parameter comes with the first step in the spin coating process and is the deposition of the solution onto the sample [47]. The solution can be deposited in such a volume that it fully covers the film, or just a smaller area, preferably in the centre of the substrate. The solution could either be deposited before the spinning starts, or as the substrate is already rotating depending on the material and the underlying film. The concentration and amount of the solution are important factors affecting the final film thickness.

The second parameter that can be tuned is the acceleration of the substrate to its final rotation speed [47]. During this stage the solution spreads out onto the film, and part of the solution will flow off the sample. When the film is thin enough it will fully co-rotate with the sample, and as the final rotational speed is reached the shear drag forces will balance the rotational acceleration and the film will be uniformly thin. Depending on the acceleration the spreading and overflow of the solvent will be more or less aggressive.

The third parameter comes with the final speed and time of the rotation at constant speed [47]. At this stage film thinning occurs gradually, both because of the rotation, but can also be partly due to evaporation of volatile solvents. As the film gets thinner the evaporation will eventually dominate the thinning of the film. The fluid thickness of the film is uniform throughout the process.

The final step in the creation of the thin films is often to further evaporate any eventual solvent by placing the film on a hotplate at a temperature higher than the boiling point of the solvent for a certain amount of time.

4.1.2 Cleaning with sonicator and UV-Ozone treatment

A sonicator, or ultrasonic cleaner, is a device that sends sonic waves above 20 kHz through a fluid in which the sample is immersed [48]. The high frequency vibrations cause so called cavitation bubbles, which are not visible to the naked eye, to form in the solution. Cavitation bubbles can grow rapidly and then collapse, thus causing an intense flow of liquid filling the void after the bubble. The gas inside the bubble can reach high temperatures, around 5000 K in the case of water. When the cavitation bubbles implode close to the surface of the substrate, the quick flow of liquid and the local heat will dislodge contaminants from the substrate, and hence clean it.

UV-Ozone treatment is the next step in the cleaning process, and is a method that has been used for a long time [49]. UV-light is high energy light that can decompose organic molecules, and can therefore be used to clean precleaned surfaces from organic molecules. The substrates are put in a closed chamber where they are illuminated by UV-light at two wavelengths. In the chamber, ozone is produced from oxygen which absorbs one of the wavelengths of the UV-light. The other wavelength will destroy the ozone forming atomic oxygen. This atomic oxygen will react with the organic compounds which have been excited and/or dissociated by the UV-light. As these compounds react with the atomic oxygen they become simpler volatile molecules, such as CO_2, H_2O, N_2 and are hence leaving the surface.

4.2 Characterisation of solar cells

When characterising the performance of solar cells there are a number of parameters that should be accounted for [29]. Originally these parameters were used to describe the function in Silicon solar cells, and although the design of a PSC differs significantly, the same parameters can still be used to evaluate their performance, such as the power conversion efficiency, the open circuit voltage, the short circuit current and the fill factor [29, 50]. These parameters and their significance in terms of physicals processes in the SC will be explained below.

When a cell is measured, it is illuminated by a controlled light source, and the current output from the cell is measured as a function of the potential over the cell [50]. One way to think about it is that the resistance of the load in the circuit (see figure 2.1b) is varied as the current and voltage is registered. The resistance of the load is varied from 0 Ohm, thus the cell is in a short circuit, to infinity, and thus equivalent to the cell being in an open circuit. The I-V curve obtained in this case characteristically looks as is seen in figure 4.1a where J_{SC} is the short circuit current, and V_{OC} is the open circuit voltage. These are two of the parameters important for characterisation of a solar cell and are explained further below.

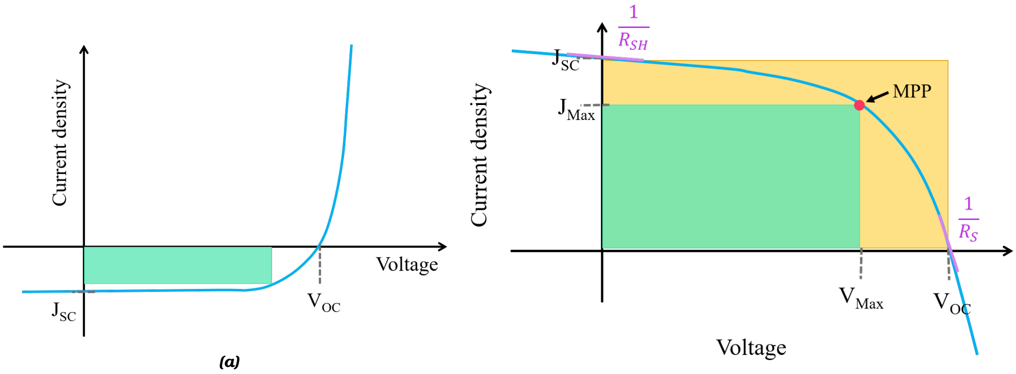

(a)

(b)

Figure 4.1: *Illustration of an I-V curve measured of a solar cell.* ***a)*** *The general shape of an I-V curve as given from the software measuring the cell.* ***b)*** *The I-V curve representation when the solar cell is considered as a power source, with the J_{SC} as a positive value by definition.*

As showed earlier, a solar cell will generate free carriers when illuminated, and the carriers will produce a current flowing through an external load. The amount of generated free carriers will be proportional to the incident radiation intensity, and hence the current produced internally by the cell is also linearly proportional to the solar radiation [50]. This internally generated current is also called the short circuit current J_{SC}, and is equivalent to the current that would be measured in a short cut circuit with the cell and is thus obtained when the potential over the cell is 0 V, as can be seen in figure 4.1a.

The open circuit voltage is the potential that is reached in the cell when the carriers do not flow in the circuit [50]. What happens in a cell under illumination at this point is that carriers are generated and will flow to the ETL and HTL respectively. Since the carriers cannot flow out of the cell they will be accumulated in the ETL and HTL respectively, and hence creating a potential over the cell. At a certain point, the potential will be so large, that newly generated carriers will be repulsed by the accumulated carriers and recombine in the absorbing layer. Then then maximal potential has been reached, which is the V_{OC}. Since the circuit is open, no current can flow, and hence V_{OC} is found where the current is 0 A on the I-V curve in figure 4.1a.

When zooming in on around the area marked by the green rectangle in figure 4.1a, some more important parameters can be defined [50]. When defining these parameters, the solar cell is considered a power source, and therefore the current is defined as positive instead of negative as was the case before. Therefore the current axis is switched, and figure 4.1b is obtained. At each point along the curve, the power output of the cell is calculated as follows [29]

$$P(V) = V * I(V) \tag{4.1}$$

The maximum power output per unit area from the cell is given at the maximum power point (MPP) indicated in figure 4.1b and is given as [29]

$$P_{MPP} = V_{Max} * J_{Max} \tag{4.2}$$

Another important parameter is the so called fill factor (FF) which can be illustrated as the ratio of the green and the yellow rectangle in figure 4.1b, giving an indication of the ratio between the MPP and the maximum theoretical power from the cell, given by $J_{SC} * V_{OC}$. such that [29]

$$FF = \frac{P_{MPP}}{J_{SC}V_{OC}} = \frac{J_{Max}V_{Max}}{J_{SC}V_{OC}} \tag{4.3}$$

The solar cell power conversion efficiency (PCE) can then be defined as the ratio between the maximum output power and the power from the incoming light (P_{in}), and is thus expressed as [29]

$$PCE = \frac{P_{MPP}}{P_{in}} = \frac{FFJ_{SC}V_{OC}}{P_{in}} \tag{4.4}$$

The two final parameters that can be of interest originate from resistances in the cell, causing electronic losses [29]. The resistances are summarised into two factors, the series resistance R_S and the shunt resistance R_{SH}. These two are illustrated in figure 4.1b in purple. The shunt resistance gives a measure of selective blocking, and has ideally a high value, while the series resistance ideally has a low value.

One final aspect that is considered when analysing solar cells is a phenomena called hysteresis, and it is illustrated in figure 4.2 [51]. What can be observed is that when the cell is scanned from a low voltage to a high voltage (forward) the maximum output power is lower than when the cell is scanned from a high to a low voltage (reverse). Part of the reason is due to low carrier mobility in some of the layers and low shunt blocking properties, but some uncertainties concerning the origin of the effect remain [29]. Ideally the hysteresis should be minimised to ensure an equal PCE regardless of the scanning direction.

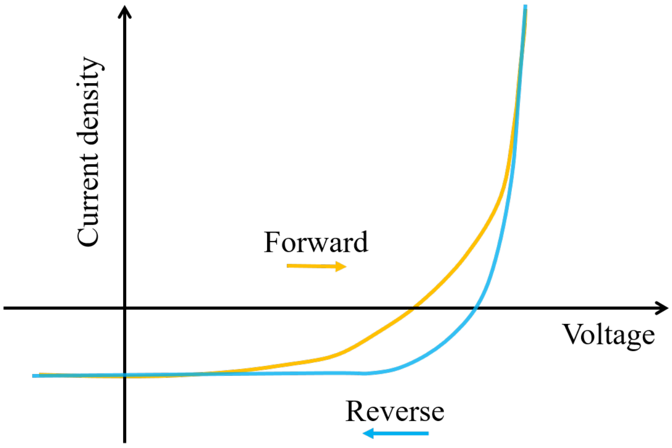

Figure 4.2: *Illustration of the hysteresis phenomena in a PSC.*

4.3 Analysis methods

To characterise the function of the manufactured cells, and the layers within the cell a number of analysis methods are used. In this section the analysis methods that have been used throughout the project and that are not considered as general knowledge will be explained. The section will be mostly oriented around the working principle of the analysis methods and the main components in the equipment used.

4.3.1 Solar cell measurements

When measuring the efficiency of a solar cell, the cell is illuminated by a computer synthesised spectrum [52]. This spectrum is standardised and accepted as a worldwide reference, and it is called the air mass 1.5 (AM 1.5) spectrum. Based on an average of yearly atmospheric conditions at mid-latitudes, the AM 1.5 spectra is representative for the irradiance of the sun on a clear day. The spectra has an intensity of 1000 W/m^2 and the cell is to be measured at ambient temperature. If the cell was to be installed in real life, the intensity would most likely be lower and the cell temperature higher, thus the conditions in the measurement are labelled 'peak conditions'.

During the measurement, a mask is applied to the cell such that only a central area with a well-defined size is measured [52]. When the area of the measured cell is known, the incoming power can be calculated, and hence also the efficiency of the cell. During the measurement, the potential over the cell is swept over an interval (recall the comparison with an imaginary load of varying resistance from earlier) at a certain speed, and the response in current from the cell is measured [53]. From this measurement the power conversion efficiency, fill factor, short circuit current, open circuit voltage, maximum power, and shunt as well as series resistance can be obtained.

4.3.2 Dynamic light scattering

Dynamic light scattering (DLS) is a method that can be used for determining the size of colloidal particles in suspension [54]. DLS method makes use of the light scattering that occurs when light interacts with particles, as well as the Brownian motion of particles in suspension. Because of the combination of these two properties it is possible to measure sizes of particles smaller than the wavelength of the light (λ) used. To measure the particle size, a laser beam is led through the suspension which is placed in a cuvette, and the scattered light is detected, as is illustrated in figure 4.3.

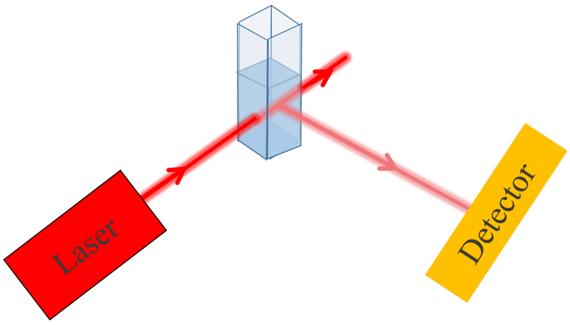

Figure 4.3: *Illustration of the principle behind dynamic light scattering*

The intensity of the scattered light depends on the scattering angle and the observation time, since the colloids move in a random walk due to the Brownian motion process [54]. Each particle will scatter light and thereby act as a secondary source of light. As the particles move randomly in the solution, the distance the light travels from the particle to the detector will vary. The light waves scattered from the particles will interfere with each other, and thus the intensity of the light will vary randomly. The detector will therefore observe speckles of light. Depending on the size of the particles, their speed of motion will vary, and hence the intensity of the speckles vary accordingly. That is, large particles will have a slower Brownian motion, resulting in a slowly fluctuating intensity signal. From knowledge about the viscosity and refractive index of the solvent it is thereby possible to obtain the particle size from the scattered light signals.

Another value that can be of interest regarding colloids in suspension is the so called zeta-potential [55]. Colloids that are naturally charged can interact due to attractive van der Waals forces, but also repulsed by a formed double layer of charged molecules at the surface of the colloids. The balance between these forces will determine if the colloids tend to aggregate into larger complexes or not. The zeta-potential is the potential between the compact and diffuse layer in the double layer at the interface between the colloid and the surrounding liquid, and gives a measure of the tendency of aggregation of the particles [56]. Thus, a high value of zeta potential indicates a lower inclination of the particles to aggregate, since the repulsive forces between them will be strong. Furthermore, the zeta potential is sensitive to pH and generally a lower pH is equivalent to lower zeta potential, and thereby more aggregated particles [57].

4.3.3 Cyclic Voltammetry

Cyclic voltammetry is an electrochemical method suitable for investigating e.g. bulk properties of materials on an electrode [58]. A common setup for a cyclic voltammetry measurement, is a three electrode setup containing a working electrode (WE), counter electrode (CE) and a reference electrode (RE) immersed in an electrolyte. An example of a three electrode system with the components used in this project is seen in figure 4.4**a**. The potentiostat controls the potential over the WE versus the RE. The potential is linearly scanned in a cyclic manner, which is from the initial potential (often the lowest potential) to the switching potential (often the highest potential of interest) and back to the initial potential. The output from the measurement is the current flowing in the cell resulting from the potential scan, resulting in a current vs. potential (IV) referred to as a voltammogram. A typical shape of a voltammogram is seen in figure 4.4**b**.

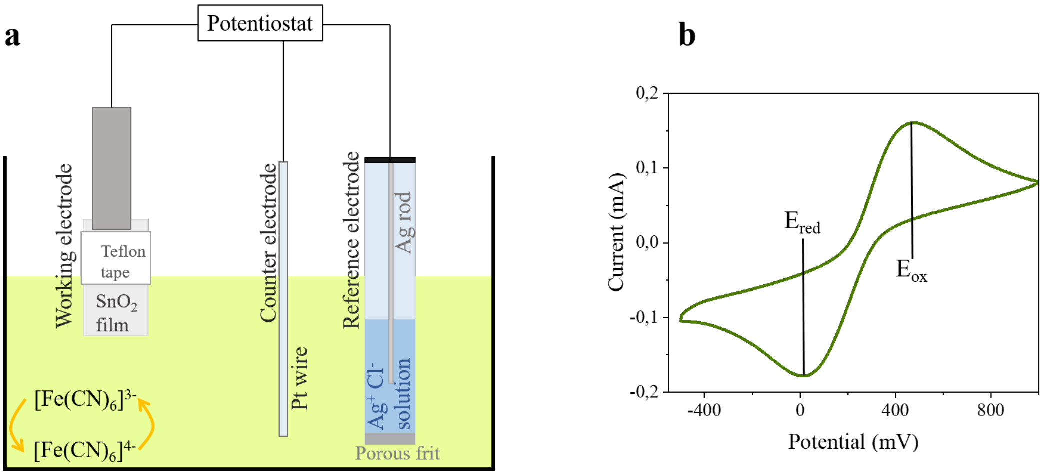

Figure 4.4: *Important concepts for cyclic voltammetry.* ***a****, The three electrode system setup with working electrode, counter electrode, reference electrode and the electrolyte.* ***b****, Illustration of a voltammogram where the reduction and oxidation waves are highlighted.*

The voltammogram in figure 4.4**b** is obtained due to redox reactions at the WE and CE surfaces [59]. As the potential is swept over the WE in the cycle, the ion complexes in the electrolyte will be reduced and oxidised. At the oxidation potential (E_{ox}) the ion complex, which in figure 4.4**a** is $[Fe(CN)_6]^{3-}$, will be oxidised to $[Fe(CN)_6]^{4-}$. A peak in current is reached as all the ion complexes close to the electrode surface are reduced. The current is due to electrons flowing from the CE to the WE. The current becomes diffusion limited when the potential is increased from E_{ox} as ion complexes must diffuse to the electrode surface to contribute to the current, hence the current decreases. As the potential is switched the current continues to decrease due to diffusion limitations until the reduction potential, (E_{red}), where a new peak is observed. The new peak is due to reduction of $[Fe(CN)_6]^{4-}$ to $[Fe(CN)_6]^{3-}$ at the WE surface, as electrons flow from the WE to the CE. As the potential is continuously decreased the process again becomes diffusion limited, and the (negative) current decreases.

4.3.4 Scanning electron microscopy

Scanning electron microscopy (SEM) is a technology used to image surfaces and surface phenomena of materials [60]. Using this technique samples can be visualised with a spatial resolution of 1 nm, giving information for example about the topography, morphology, composition and orientation of grains in the sample. The working principle of the SEM is most simply described by an electron beam of high energy electrons hitting the sample, after which the electrons and X-rays emitted by the sample as a result of the interaction with the electron beam are analysed. From this analysis an image of the sample can be obtained.

When analysing a sample it is mounted on the SEM sample holder, which is a metal stub [60]. The sample is fixed on the stub most often using carbon tape. Since the sample is being hit by electrons it is of importance to avoid overcharging of the sample surface. Therefore the sample must be conductive. Since the sample surfaces in this project will be either SnO_2 or PSK, which are both conductive materials this will already be fulfilled. In case the sample of interest is non-conductive, then a conductive material such as graphite or a metal can be sputtered on top of the surface to make it conductive. The stub is placed inside the instrument, where it is put under vacuum. The vacuum is necessary to avoid interactions between the electron beam and gas molecules. Once the sample is put under vacuum the measurement can start.

The measurement starts as the high energy electron beam hits the sample. As the electrons hit the sample three main processes can take place [61]. The first is that the incoming electrons collide with and excite the electrons of the sample. The excited electrons are often referred to as secondary electrons (SEs) and will have a low energy (about 5 eV) compared to the electrons in the electron beam (about 100 eV). Because of their low energy, only the SEs closest to the surface of the sample, about 10 nm from the sample surface, will be detected as they leave the sample. The detected SEs are used to image the topography of the sample. The second process of importance occurs as the incoming electrons excite an electron in the material, and the excited electron relaxes back to its ground state. As the electron relaxes, X-rays are emitted. X-rays of different wavelengths are emitted depending on the material that is analysed, thus creating a fingerprint for the specific material. The X-rays are detected and the information is used to distinguish the materials in the sample. The third process occurs as the incoming electrons collide with the atoms of the material and get reflected or back scattered. The intensity of back scattered electrons (BSEs) increase with the size of the nucleus, thus information about the material and about the position of the centre of the atom can be obtained from the BSEs.

For the SEM technique the electron beam is scanned across the investigated area to get and image of the surface [60]. The three main sources of information used to image the sample are the SEs, the X-rays and the BSEs. If overcharging of the sample occurs, that is if electrons get accumulated at the sample surface, the image will get distorted and appear as glowing because of the high amount of electrons present. Therefore, as previously mentioned, it is of importance that the sample is conductive. Since the electrons that are excited leading to the SEs are continuously replaced by incoming electrons, the method is non-destructive, and a same sample can be analysed multiple times.

4.3.5 Atomic force microscopy

Atomic force microscopy (AFM) is a method used to capture 3D topographic images of a 2D surface [62]. With modern equipment it is possible to obtain atomic resolution with AFM, to resolve monoatomic steps in the z-plane and observe lattice structures and surface defects in the x-y-plane. Simply described the AFM setup consists of a movable cantilever with a tip that is in contact with the analysed surface, a laser source, a photodiode that registers a laser beam reflected from the cantilever, and a detector that registers signals from the photodiode and forwards feedback signals to adjust the position of the cantilever. These components can be seen in figure 4.5.

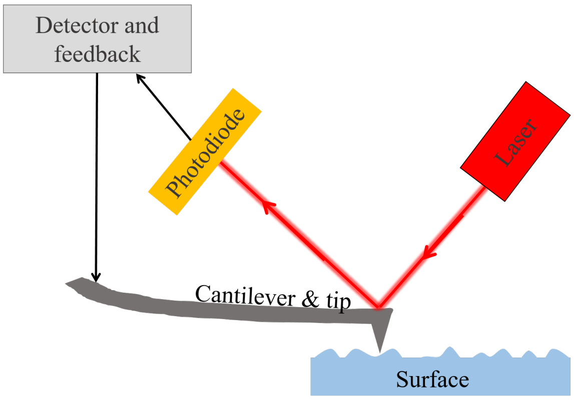

Figure 4.5: *Illustration of the main components in a AFM equipment and the signal routes.*

During the measurement, the tip is scanned over the surface with high precision in a back and forth manner such that eventually the whole surface of interest is covered. As the tip moves along the sample, it interacts with the surface [62]. This interaction is due to repulsive and attractive forces between the tip and the surface, causing the cantilever to deflect [63]. The deflection is measured by tracking a laser beam, which reflects upon the cantilever. As the cantilever moves across the surface, the surface topography will affect the interaction between the tip and the surface. Thus the deflection of the cantilever will change, and this change will be registered in the photodiode trough the laser. By altering the position of the cantilever, the signal is brought back to its nominal value. Through this adjustment, it is possible to create the surface profile of the sample.
From the sample profile obtained in the AFM measurement, it is possible to calculate the average surface roughness of the sample. The surface roughness R_q is given by first evaluating the mean value, μ, of the height, z, across the $x-y$-plane of the sample as follows [64]

$$\mu = \frac{1}{MN}\sum_{k=0}^{M-1}\sum_{l=0}^{N-1} z(x_k, y_l) \tag{4.5}$$

Then the surface roughness is given by the square root of the standard deviation of the height according to [64]

$$R_q = (\frac{1}{MN}\sum_{k=0}^{M-1}\sum_{l=0}^{N-1}[z(x_k, y_l) - \mu])^{1/2} \tag{4.6}$$

where M and N are the amount of data points in x- and y- direction respectively. By this calculation the surface roughness can be calculated and compared between different substrates.

4.3.6 Contact angle measurement

A contact angle measurement is a method that can be used to evaluate the effects of surface treatment in terms of wettability, where wettability describes how well a liquid spreads on a surface [65]. When a liquid comes in contact with a surface, the liquid will experience adhesive forces at the contact area between the drop and the surface. These adhesive forces will favour spreading. On the other hand the spreading will be counteracted from cohesive forces within the liquid. The contact angle is determined when these two forces balance each other.

To measure the contact angle, the silhouette of a backlit drop is imaged as it is deposited onto a surface [66]. The image is taken from slightly above the horizon to better image the correct point of contact. A line is estimated along the surface of the drop at the point of contact at the edge to determine the contact angle. An image of how the angles are measured can be seen further down in figure 6.12. It has been shown that drop size can affect the measured value of the contact angle, to various extents depending on the liquid and the substrate [67, 68]. Hence it is of good practice to keep the drop volume constant if samples are to be compared with each other.

4.3.7 X-ray diffraction

X-ray diffraction (XRD) is a technique that can be used to determine the parameters of crystalline samples [69]. Typical properties that can be investigated are structure characteristics of the crystal and material contents. The most common way of performing XRD is to use a sample in powder form, but XRD can also be performed on solid thin films [70]. The working principle of the method is that X-rays incoming on a sample will be diffracted due to the crystallinity of the sample, and the diffracted pattern is detected.

Diffraction is a phenomena occurring when incoming light excites electrons in a crystalline structure, after which the electrons relax to their ground state by emitting light of the same wavelength as the incoming light in all directions [69]. Since the atoms are arranged in a crystal lattice, the emitted light will interfere constructively and destructively in an ordered manner, thus creating wavefronts that are in phase radiating out from the sample.
The diffracted light can occur as a reflection under certain conditions described by Bragg's law which states that [69]

$$2dsin(\theta) = n\lambda \tag{4.7}$$

where d is the distance between two parallel planes in the crystal, θ is the angle of the incoming and outgoing light, n is an integer and λ is the wavelength. A Lattice and rays obeying Bragg's law are illustrated in figure 4.6.

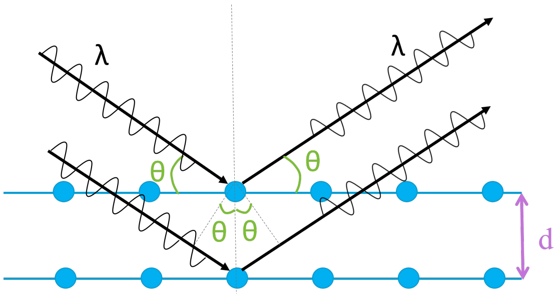

Figure 4.6: *Rays interacting with a crystal lattice and fulfilling Bragg's condition*

For large incoming angles the penetration depth of the light can penetrate up to a few micrometers into the sample [71]. This is unpractical for investigating thin films where only a few hundred nanometers are of interest. Therefore small grazing angles are selected, usually $< 10^\circ$, such that the measurement investigates the near surface region. By varying the angle of the incoming light, different atoms in the material will fulfill the Bragg condition and thus a number of angles will yield high intensity diffracted peaks. Depending on the crystal structure, some characteristic peaks will be obtained thus leaving a fingerprint for that structure [72]. From the Bragg condition the lattice parameters of the crystal structure can be calculated, and from there the material can be identified.

4.3.8 Photoluminescence spectroscopy

Photoluminescence (PL) spectroscopy is based on fluorescence and phosphorescence from a sample [73]. Fluorescence occurs when electrons in a sample are excited and then relax to the ground state in more than one step, on the same timescale as the excitation of the sample. This means that the electron first relaxes to the excited ground state by non-radiative processes, and the relaxes to the ground state and thus emitting a photon. Since some energy is lost in the non-radiative process the light that is emitted has a longer wavelength than the excitation wavelength. The relaxation processes are fast and take place on the same timescale as the excitation. Phosphorescence on the other hand is a slower process involving the triplet electronic states [74]. Therefore phosphorescence can be observed even after the excitation source is removed.

During the PL measurement, the sample is excited by a laser, and the intensity of the emitted fluorescence and phosphorescence is detected in a so called PL spectra [75]. To excite the sample a laser is used, and a wavelength larger than or equal to the bandgap is chosen for the excitation. In the PL spectra the luminescence intensity for each wavelength is shown. From the PL spectra, properties such as optical emission efficiencies, impurity content and composition of the material can be obtained. These can be obtained from information about the luminescence intensity, and from the luminescence peaks in the spectra which are fingerprints for the materials in the sample. [73].

5 Experimental method

The manufacturing process of the solar cells can be divided into two parts, where the glass substrates are prepared for deposition of the thin films in the first part, and thin film deposition takes place in the second part. This division in methodology is also made in this chapter for simplicity. Finally the details for the characterisation of the SnO_2 films are given.

5.1 Preparing substrates

The glass sheets with FTO film on are cut into pieces measuring $9.6 * 11.2$ cm, and then carved for the final cutting with cells measuring $1,4 * 2.4$ cm, such that each piece fits $8 * 4$ cells, as can be seen to the right in figure 5.1. The cuts are done on the glass side of the glass sheets to avoid glass splinters on the FTO side. Each cut is done by placing the tip of the cutter onto the sheet, and the cutter is pushed onto the glass firmly and dragged slowly across the surface. The cuts are not carved too close to the edge of the glass sheet, to avoid cracks and splinters.

Next the glass substrate is prepared for etching away part of the FTO layer. On the FTO side of the carved glass piece, scotch tape is placed 2 mm from the carved line along one side of each cell. To save material and effort, the carved line separating two rows of cells is used, such that a gap of 4 mm along that carved line is created. The scotch tape is firmly pushed with a cotton tip onto the FTO to avoid air bubbles, and a cotton tip is used to make sure that the edges of the tape are well attached.

When the scotch tape is in place, the glass piece is put into a glass tray and a small amount of zinc powder (purum powder, Sigma-Aldrich) is spread onto the 4 mm wide FTO surfaces between the scotch tape as can be seen to the left in figure 5.1. Using a plastic pipette, 4 M HCl (ACS reagent, 37%, Sigma-Aldrich) is dropped onto the zinc causing the single replacement reaction $Zn + 2\,HCl \rightarrow ZnCl_2 + H_2$ which is a spontaneous exothermic reaction, thus generating heat. Under this reaction the FTO is etched off the glass surface. In the middle picture of figure 5.1 HCl has been dropped onto the zinc and the reaction is ongoing. The HCl is left on the FTO surface for about 1 min, then it is rinsed off with water and a rubber tip to further rub off remains of FTO. The tape is removed and the surface washed with water. After successful etching, the edges of the FTO film should be straight and even. This can be seen by the naked eye as the FTO film is slightly grey, while the pure glass is fully transparent as can be seen to the right in figure 5.1

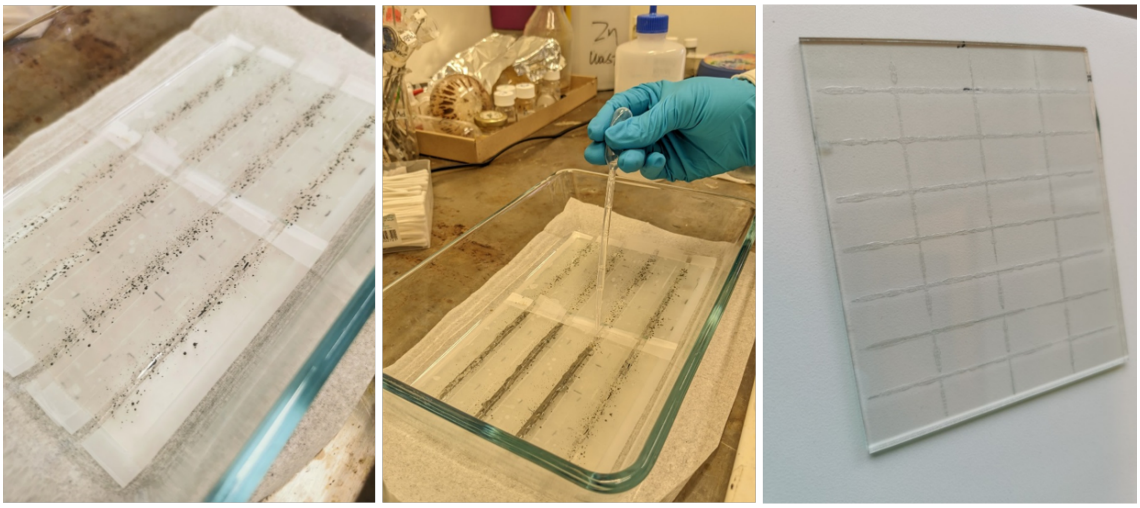

Figure 5.1: *zinc powder deposited onto the FTO (left) with 4 M HCl dropped onto the powder (middle). After the cleaning process a faint colour shift can be seen where the FTO has been etched away along every second horizontal line.*

The carved and etched glass piece measuring $9.6 * 11.2$ cm is cut into pieces measuring $9.6 * 2.8$ cm such that each piece fits $2 * 4$ cells. The cuts are made such that the 4 mm stripe of etched away FTO is along the middle carving separating the two rows of cells. The pieces are blown clean off glass splinters using air. A 10% Hellmanex III (Sigma-Aldrich) solution is prepared and the glass substrates are cleaned with a soft sponge and the Hellmanex solution, washed with water and then put into the substrate holder of the sonicator, as can be seen to the left in figure 5.2. The substrates are covered with a 2% Hellmanex solution and put in the sonicator (Branson, 3510) for 30 min, as is seen in the middle of figure 5.2. When done, the substrates are washed with water and dried with air, then covered with acetone and put in the sonicator for 20 min. The substrates are then dried with air, and covered with ethanol and put in the sonicator again for 20 more minutes. Finally the samples are dried with air. During the process, great caution to not touch the surface of the glass is taken.

Finally the glass substrates are cut into the size of the cells, while not touching the FTO side of the glass substrates. All steps up till now can be done several days/weeks ahead of the manufacturing of the solar cells, if the samples are stored well and protected from dust. However, the steps described ahead and in the next section are to be performed on the same day as the manufacturing of the cells, since sensitive chemistry is involved.

The substrates are cleaned from glass splinters using pressured air. The substrates are put in the UV-ozone cleaner (Ossila, E511) with the FTO side upwards for 20 min for the final cleaning step, as is seen to the left in figure 5.2.

Figure 5.2: *Glass substrates covered with ethanol and placed in holder (left) and put inside the sonicator (middle). The last step in the cleaning process is the UV-ozone treatment in the UV ozone cleaner (right).*

Immediately after the UV-ozone cleaning the substrates are taken to the next step in the process which is the spin coating of the films.

5.2 Solutions, depositing films and gold contacts

All solutions used for the films are prepared on the same day as the manufacturing of the films is to take place to avoid any ageing affects in the solutions and to ensure reproducibility.

The solution for the interfacial treatment was prepared by dissolving ammonium salt in isopropanol (Sigma-Aldrich) in ambient conditions. Four different concentrations were prepared: 0.5 mg/ml, 1 mg/ml, 5 mg/ml and 10 mg/ml. The solution was heated on a hotplate at 50 °C so that the salt would fully dissolve.

The SnO_2 solutions are prepared in ambient condition from deionised water (reagent ACS, Thermo Fisher Scientific) and tin(IV) oxide (15% in H_2O Alfa Aesar) and the ammonium salt solved in deionised water with a concentration of 6.25 mg/ml. The SnO_2 solutions all have a 1:4 ratio of SnO_2 stock solution and deionised water, and four different concentrations of the ammonium salt in the SnO_2 solutions are prepared. The four concentrations are 0.5 mg/ml, 1 mg/ml, 3 mg/ml and 5 mg/ml. The final solutions are seen in the middle photo of figure 5.3 with the reference (1:4 ratio) SnO_2 solution, 0.5 mg/ml, 1 mg/ml, 3 mg/ml and 5 mg/ml from left to right.

After cleaning the substrates with UV-ozone, the substrates are cleaned from dust with air. On the opposite side of where the FTO was etched away, 2 mm of the FTO film is covered with scotch tape, such that the SnO_2 film would not cover the full surface. In a later step the small gold contact will be deposited on the covered FTO film. The tape is pushed firmly onto the surface using a cotton tip. The substrate is then cleaned with air and is placed on the spin coater. The inside of the spin coater is covered with aluminium foil to protect its surface, and to protect the sample from chemical residue from earlier experiments as is seen to the left in figure 5.3. Using a micropipette 250 μl SnO_2 solution is deposited onto the substrate making sure the solution covers the surface well. The settings of the spin coater are 5000 rpm with an acceleration of 3000 rpm/s and program length 30 s. After the spin coating the samples are annealed on a hot plate at 150deg for 40 minutes, as seen to the right of figure 5.3.

Figure 5.3: *SnO_2 solution deposited onto a substrate on the spin coater (left), the SnO_2 solutions with different concentrations of the ammonium salt (middle) and substrates coated with SnO_2 solutions annealing on the hotplate (right).*

On the cells where the interfacial treatment was added, 100 μl solution was deposited onto the cooled down SnO_2 film. The substrate was then spin coated for 20 s with 4000 rpm and the acceleration 2000 rpm/s.

The PSK solution is prepared in a nitrogen glovebox with low oxygen concentration in the air. The PSK is prepared from methylammonium iodide (MAI, greatcells solar materials) and lead(II) iodide (PBI_2, Tokyo chemical industry co.) solved in dimethyl sulfoxide (DMSO, 99.7+% acros organics) and dimethylformamide (DMF, 99.8% thermo scientific). The PSK solution is then brought outside of the glovebox and the film is spin coated in ambient condition. Once the substrates have cooled down after the annealing of the SnO_2 film, they are cleaned with UV-ozone for 20 min, then cleaned with air and placed on the spin coater, which is again covered in aluminium foil. The PSK film is coated in a two-step process. The first step in the spin coating programme lasts for 10 s with 2000 rpm and an acceleration of 200 rpm/s. The second step lasts for 25 s with 6000 rpm and an acceleration of 2500 rpm/s. Using a micropipette 40 μl of PSK solution is spread out on the substrate and the spin coating programme is started. When 15 s remains of the second step, 100 μl of chlorobenzene is deposited onto the spinning sample. After spin coating the substrate is annealed on a hotplate at 100deg for 40 minutes. The dark brown/black colour of the PSK film becomes gradually visible after that the substrate is placed onto the hotplate, as is seen to the left in figure 5.4.

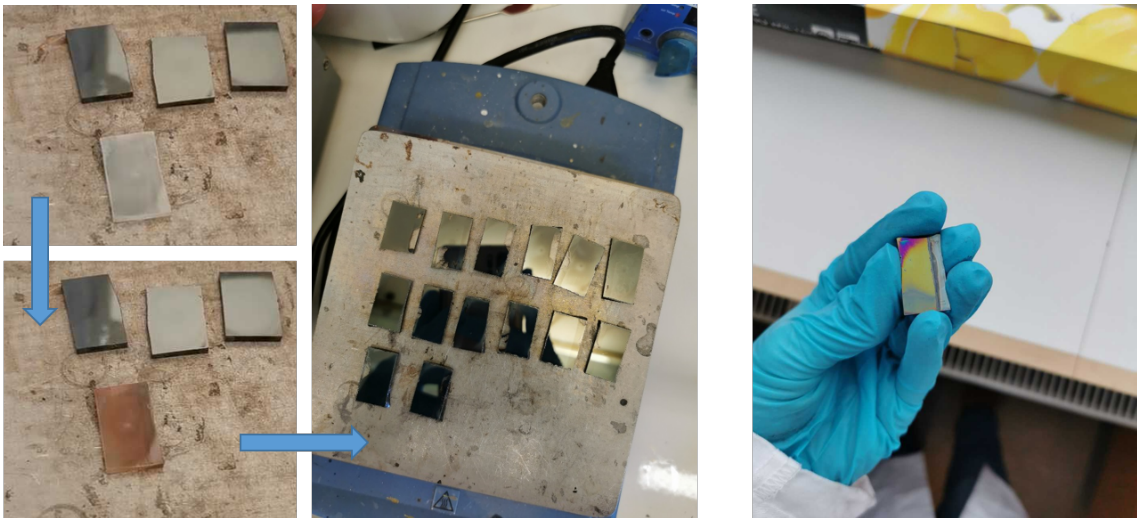

Figure 5.4: *After spin coating the PSK film is still highly transparent, but as the substrate is heated up the crystals gradually form and the film goes from dark orange/brown to shiny and dark brown/black (left). The spiro is deposited onto the PSK film, and 2 mm of the film is removed where the gold electrode will later be placed.*

The spiro solution was prepared in the nitrogen glovebox from spiro-MeOTAD (Sigma-Aldrich) powder dissolved in chlorobenzene doped with 4-tert-butylpyridine (tbp, 98% Aldrich) and bis(trifluoromethylsulfonyl)imide lithium salt (LiTFSI, Sigma-Aldrich) solved in Acetonitrile (99.8% Sigma-Aldrich). The spiro solution was then brought outside the glovebox and the spin coating was done in ambient condition. When the substrate with the deposited PSK film had cooled down to ambient temperature it was cleaned with air and placed on the spin coater. The program was set to run for 20 s with 4000 rpm and 2000 rpm/s. Using a micropipette 35 μl spiro solution was deposited onto the PSK surface during as the sample started spinning within the first two seconds of the program.

To prepare the cells for deposition of gold electrodes, the PSK and spiro is removed using gamma-butyrolacetone (GBL, Sigma-Aldrich) along the 2 mm wide stripe where the SnO$_2$ does not cover the FTO as is shown to the right in figure 5.4. The cells are then dried with air. The evaporator (Leica EM MED020) is loaded with 150 mg of gold in a wolfram boat as seen to the left in figure 5.5. The cells are placed in the template with the stripe of removed PSK along the long stripe in the template as seen in the middle of figure 5.5. During the evaporation 80 m of gold is deposited onto the cell and the final result can be seen to the right in figure 5.5.

Figure 5.5: *The gold evaporation is done with 150 mg gold placed in a wolfram boat (left). The samples are placed in the template with the long thin opening along the area where the PSK has been removed (middle). After evaporation 80 nm of gold has been deposited onto the cell (right).*

The manufactured cells are tested in the solar cell simulator (wavelabs sinus 70) with the setting AM 1.5G, with one sample area measured at a time. In between the measurement and the finalising of the cells, they are stored in a drybox which has low moisture in the air to avoid degrading of the PSK.

5.3 Characterisation of tin oxide films

For the characterisation of the SnO_2 film and the PSK film, additional samples are prepared. The films are prepared as described above, but only until the film of interest has been deposited. This means that for the SnO_2 films only the SnO_2 is deposited on the substrate, and for the PSK film, only the SnO_2 and the PSK are deposited. For the characterisation of the films the function of the cell is not of importance. Hence the FTO is not covered by scotch tape along the edge as was done previously, which facilitates the manufacturing process and maximises the analysis area. The characterisation methods are performed within a few days of the manufacturing of the films to minimise the risk of ageing effects of the materials.

The DLS is performed on a Zetasizer nano series from Malvern. Each sample is measured eight times, and each measurement is an average of three scans with no delay in between the scans. The same SnO_2 solution is used and aged throughout all measurements, stored in a cabinet in ambient condition in between measurements. The pH measurement is done with freshly made solutions by dropping a small amount of each condition onto the pH paper and directly noting the results.

For the cyclic voltammetry the electrolyte was 1 mM potassium ferricyanide ($K_3Fe(CN)_6$) and 1 mM potassium ferrocyanide ($K_4Fe(CN)_6$) dissolved in the supporting electrolyte 0.5 M potassium chloride (KCl) aqueous solution. The Reference electrode (RE) is a platinum rod and the working electrode (WE) is the SnO_2 film to be investigated. The surface area of the samples is controlled by measuring a $1 * 1.2$ cm rectangular area, and covering the rest of the film with Teflon tape as is seen to the right in figure 5.6. The electrodes are immersed in the electrolyte as seen to the left in figure 5.6 and a tube with nitrogen gas (N_2) is put into the electrolyte to minimise the amount of oxygen in the solution. The N_2 gas flows through the electrolyte for five minutes before the measurement starts, then the tip is brought above the electrolyte surface to keep a N_2 gas pressure above the surface.

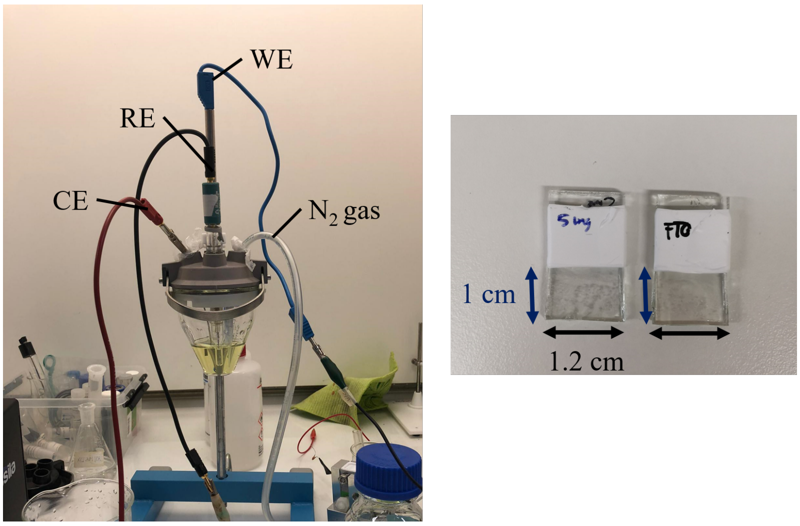

Figure 5.6: *The setup for the cyclic voltammetry measurement with a graphite counter electrode (CE) a Ag+/AgCl reference electrode (RE), the working electrode (WE) with the film fastened and a tube with nitrogen gas (N_2) connected (left). Two samples where the active of 1.2 cm^2 is below the teflon tape (right).*

The contact angle measurement was performed with an Ossila setup, where a video of the PSK drop landing on the surface was recorded. From the recording, then contact angle at the first instant where the drop was in full contact with the surface was measured. One such picture is illustrated in figure 5.7 where PSK has been dropped onto a film with 0.5 mg/ml additive and no UV-ozone treatment. The PSK solution is the same as when making the PSK films and is dropped manually from a syringe.

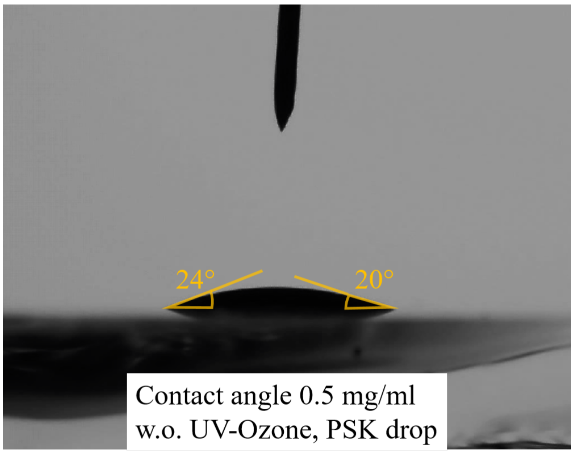

Figure 5.7: *Illustration of how the contact angle is measured from the recording of the PSK drop falling onto the surface.*

For the PL measurement, samples with the structure glass/FTO/SnO_2/PSK were prepared. The samples were prepared in ambient condition concurrently with two samples of each condition. The samples were inserted in a FLS1000 modular system with a 450 W xenon lamp as excitation source with 520 nm. The light strikes on the PSK side of the sample as the PL spectra is recorded. Between the manufacturing and the measurement the samples were stored in a dark and dry environment in a drybox.

The AFM, SEM and XRD measurements are performed in a clean lab environment. For AFM films with the structure glass/FTO/SnO_2 were prepared and stored in ambient condition until the measurement. The equipment used is PSIA XE150 with contact AFM.

For SEM two kinds of films were prepared to investigate both the PSK and the SnO_2 structure. For investigating the PSK substrates with glass/FTO/SnO_2/PSK were prepared in ambient condition and stored in a drybox for dry and dark storage until the measurement. For investigating the SnO_2, substrates with glass/FTO/SnO_2 were prepared and stored in ambient condition until measured. The equipment used is a Zeiss LEO1550 with Oxford AZtec EDS and the images were obtained using a Schottky field emission gun. to connect the conductive surfaces to the carbon tape on the sputter, a small piece of carbon tape was put on one edge of the sample.

For the XRD measurement, substrates with glass/FTO/SnO_2/PSK were prepared in ambient condition and stored in a drybox until measured. The instrument used for the XRD measurement was a Siemens D5000 Bragg-Brentano with Cu K-alpha radiation.

6 Results and discussion

The results in this chapter are presented in two parts, first the PCE and parameters of the SC manufactured during the project, and then the characterisation analysis of the ETL/PSK interface. For all the box plots presented the box is defined by the 25th and 75th percentile lines. The line within the box is the median, equivalent to the 50th percentile. The whiskers are found using a coefficient of 1.5 multiplied with the inter-quartile length, which is the distance from the 25th percentile to the 75th percentile.

There are two important things to keep in mind when reading the results in this project. The first one is that the presented values for PCE, FF, J_{SC}, and V_{OC} are for the reverse scan. The second note is that the purpose at this stage of the research is to find the highest possible efficiency reachable for a certain combination of materials. This means that malfunctioning cells yielding low PCEs or short circuit will not be presented. The reasoning behind this, is that the fabrication methods are not fully optimised yet and hence not all cells will be perfectly manufactured and thus not fully representing the potential of the materials it contains. Moreover, if a cell at this stage is fabricated and yields a high PCE, that PCE will be reachable or even exceeded again with some more tuning in the fabrication procedure. Therefore the purpose of the PCEs presented here is to give an indication of the potential of the materials used, and hence the malfunctioning cells will be excluded.

6.1 Characterisation of cells without interfacial treatment

The PCE of the set of cells manufactured without any additive in ambient condition was measured, and the result is seen in figure 6.1.

a

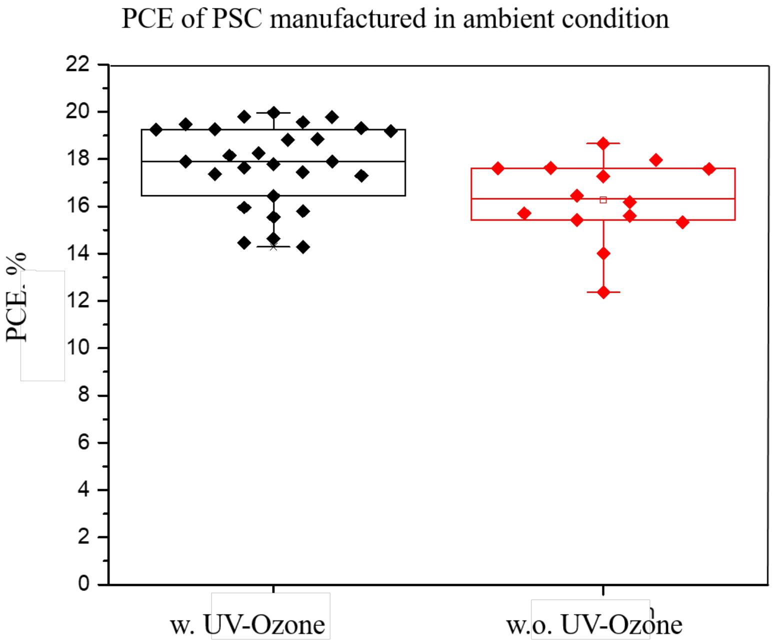

b

	PCE (%)	FF (%)	Jsc (mA.cm^-2)	Voc (V)
w. UV-ozone	19.96	79.07	23.67	1.07
w.o. UV-ozone	18.66	71.79	24.46	1.06

Figure 6.1: *Results from PSC manufactured in ambient condition.* ***a)*** *PCE of PSCmanufactured with (left) and without (right) UV-ozone cleaning. The cells giving PCEs over 12% are shown.* ***b)*** *Parameters for the best performing cell of each condition*

In figure 6.1a only the cells yielding PCEs over 12% are shown, since it was assumed that the cells yielding results below 12% were malfunctioning due to fabrication errors. As can be seen there is a clear difference in PCE between the two conditions, where the cells that had UV-ozone treatment before deposition of the PSK perform better, with a higher PCE in average. The parameters for the champion cell of each condition are seen in figure 6.1b. There it is clear that the cell with UV-ozone treatment has 1.3 percentage units higher PCE, which is a noticeable difference. The fill factor shows a clear increase for the cell with UV-ozone treatment, which further attributes to the good performance of the cell. The I_{SC} and V_{OC} are comparable for both treatments.

The characteristics of the I-V curve were in general good, with not too much hysteresis. The I-V curve for the best performing cell with UV-ozone treatment is seen in figure 6.2 as a representative for the batch.

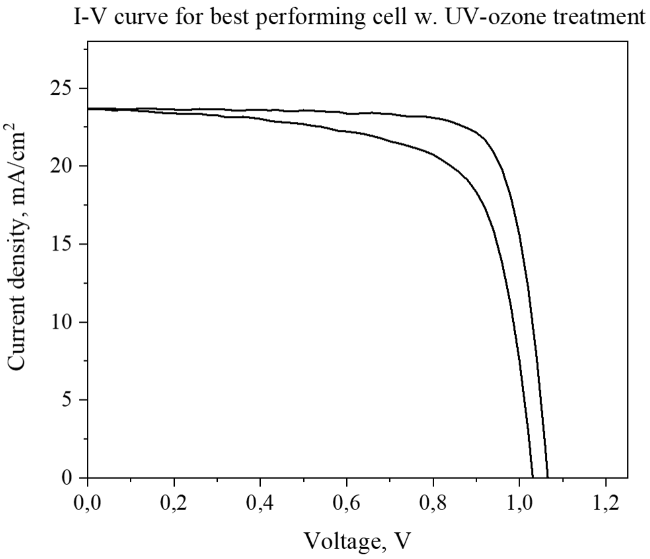

Figure 6.2: *I-V curve of the best performing cell with UV-ozone treatment. The cell does not show severe hysteresis.*

From these results it is clear that PSCs manufactured in ambient conditions can yield high efficiencies with reproducible results, and that the UV-Ozone cleaning does have a non-negligible impact on the performance of the cell.

6.2 Characterisation of cells with interface engineering

The cells with the interfacial treatment were manufactured in ambient condition, and their performance can be seen in figure 6.3. From the PCE in figure 6.3a it is seen that the lower concentrations of the ammonium salt (0.5 mg/ml and 1 mg/ml) seem to perform similarly to the reference cell, which is the same PSC without UV-ozone treatment before the deposition of the PSK as in figure 6.1a, while the higher concentrations (5 mg/ml and 10 mg/ml) seem to yield slightly lower PCE on average than the reference. Only the cells with PCE above 12% are shown, since PCEs lower than that are rather considered as malfunctioning cells due to fabrication effects than representing the effect of the interfacial treatment.

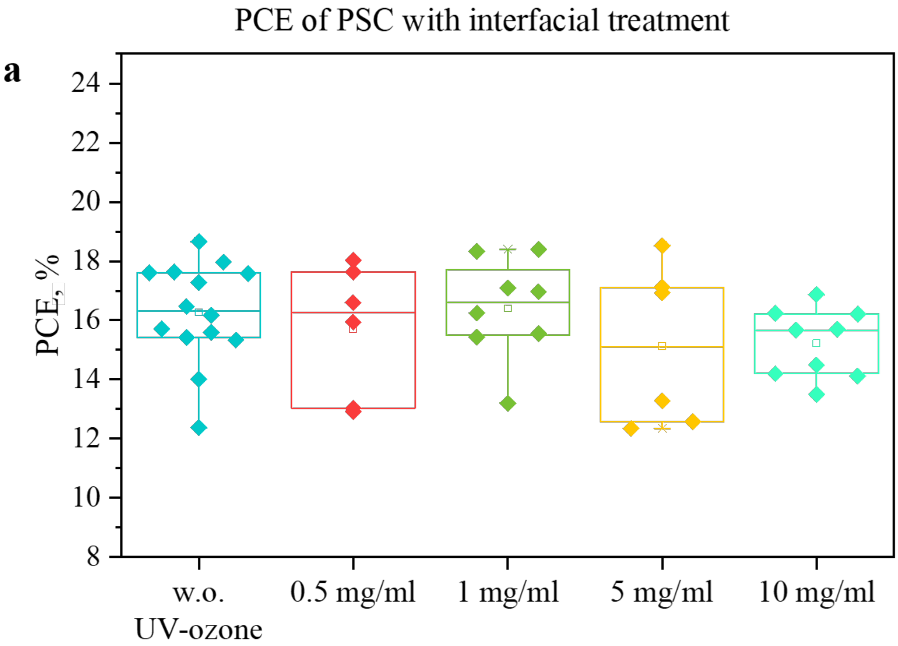

b

	PCE (%)	FF (%)	Jsc (mA,cm^-2)	Voc (V)
w.o.UV-Ozone	18.66	71.79	24.46	1.06
0.5 mg/ml	18.03	76.13	23.33	1.02
1 mg/ml	18.40	72.86	23.58	1.07
5 mg/ml	18.52	75.13	23.79	1.04
10 mg/ml	16.88	70.05	23.31	1.03

Figure 6.3: *Results from PSC manufactured in ambient condition with interfacial layer of ammonium salt.* ***a)*** *PCE of PSC with different concentrations of ammonium salt in the interfacial layer. The cells giving PCEs over 12% are shown.* ***b)*** *Parameters for the best performing cell of each condition.*

When looking at the champion parameters in figure 6.3b it is seen that the reference cell is the best performing cell, and that the cells with added ammonium salt in concentrations of 0.5-5 mg/ml have a comparable PCE, while 10 mg/ml is clearly lower. The fill factor clearly increased for samples with added ammonium salt in concentrations of 0.5 mg/ml and 5 mg/ml, while it remained comparable to the reference for 0.5 mg/ml and 10 mg/ml. The I_{SC} and V_{OC} are comparable for all samples. This suggests that the ammonium salt did not improve the charge transportation, but neither did it decrease the charge transport properties of the cell significantly. Since this did not yield a significant improvement, the ammonium salt was instead added to the bulk of the SnO_2 layer.

For the cells with the additive in the bulk there was an error made in the etching of the cells, and therefore less cells than expected worked. On the other hand, the cells that worked showed the highest efficiencies observed in this project, and those can be seen in figure 6.4a.

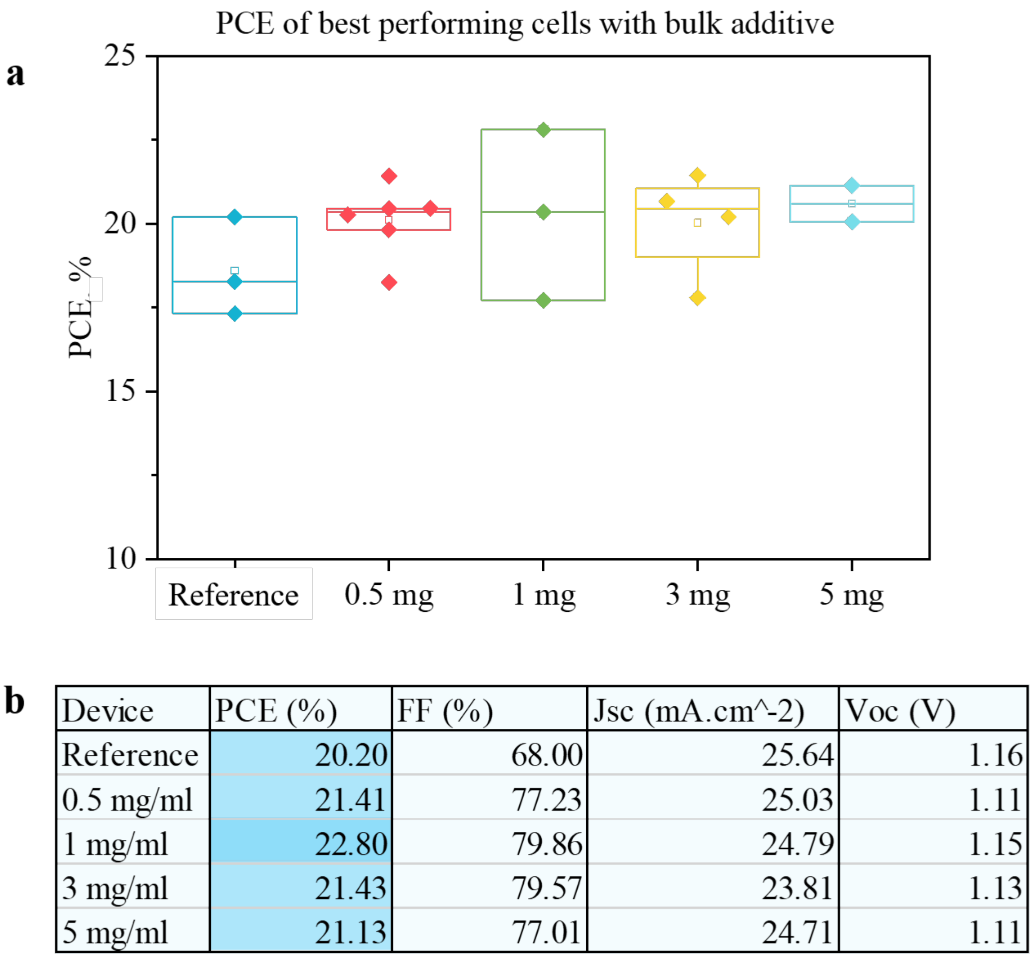

Device	PCE (%)	FF (%)	Jsc (mA.cm^-2)	Voc (V)
Reference	20.20	68.00	25.64	1.16
0.5 mg/ml	21.41	77.23	25.03	1.11
1 mg/ml	22.80	79.86	24.79	1.15
3 mg/ml	21.43	79.57	23.81	1.13
5 mg/ml	21.13	77.01	24.71	1.11

Figure 6.4: *Results from PSC manufactured in ambient condition with ammonium salt additive in the bulk of ETL.* ***a)*** *PCE of PSC with different concentrations of ammonium salt in the bulk of ETL. The cells giving PCEs over 12% are shown.* ***b)*** *Parameters for the best performing cell of each condition.*

The reference was a PSC treated with UV-ozone, and the result is similar to what has been observed earlier. It is seen in figure 6.4a that on average, the cells treated with the ammonium salt in the bulk show higher efficiencies than the reference. This is also observed when looking at the parameters of the champion cells in figure 6.4b. The PCE of the champion reference cell is the lowest one observed. The same trend is seen for the fill factor, where the highest fill factor is observed for 1 mg/ml additive. The I_{SC} and V_{OC} are comparable for all treatments, although varying a bit with no clear trend.

The I-V curves of the samples showed little hysteresis in general, and the I-V curve of the champion cell, which is the champion cell with 1 mg/ml additive is shown in figure 6.5.

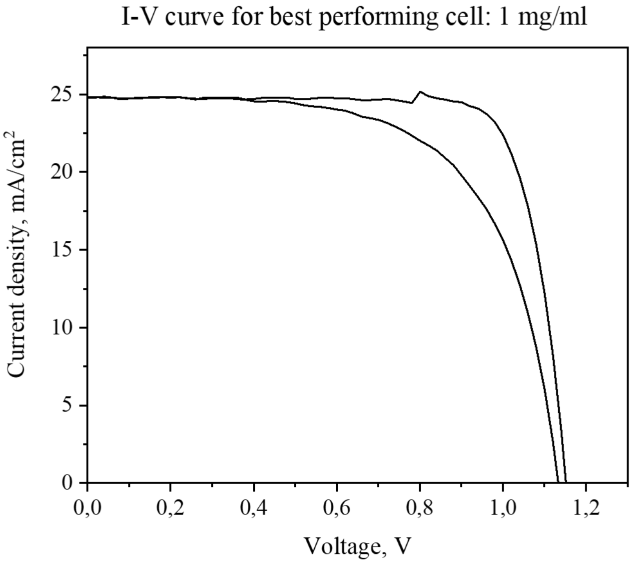

Figure 6.5: *I-V curve of champion cell with 1 mg/ml additive.*

As can be seen in figure 6.5 the cell shows some hysteresis but not too severe.

Based on the results from the cells with the bulk additive seen in figures 6.4 and 6.5, it is clear that adding the ammonium salt to the bulk of the SnO_2 layer in the PSC does improve its efficiency. However, the experiment should be repeated with more manufactured cells to gain more certainty in how big the favourable impact on the cell PCE is. To understand what causes the observed higher PCE in the cells, characterisation of the SnO_2 layer with the additive is needed.

6.3 Characterisation of films

In this project, the focus of the characterisation has been on characterising the properties of the SnO_2 films. The point of interest was to see how the properties of the SnO_2 and PSK films are affected by the ammonium salt additive, and if this change in property could explain the increased performance of the cells. It lies outside the scope of the project to investigate what mechanisms and interactions between the ammonium salt and SnO_2 have led to these changes. Therefore the results and the discussion here will not focus on the ammonium salt, but rather on the films and their properties.

The first part of the characterisation focused on the SnO_2 solution with the additive and the stability of the solution. The particle size of the solutions were measured over time and the result can be seen in figure 6.6.

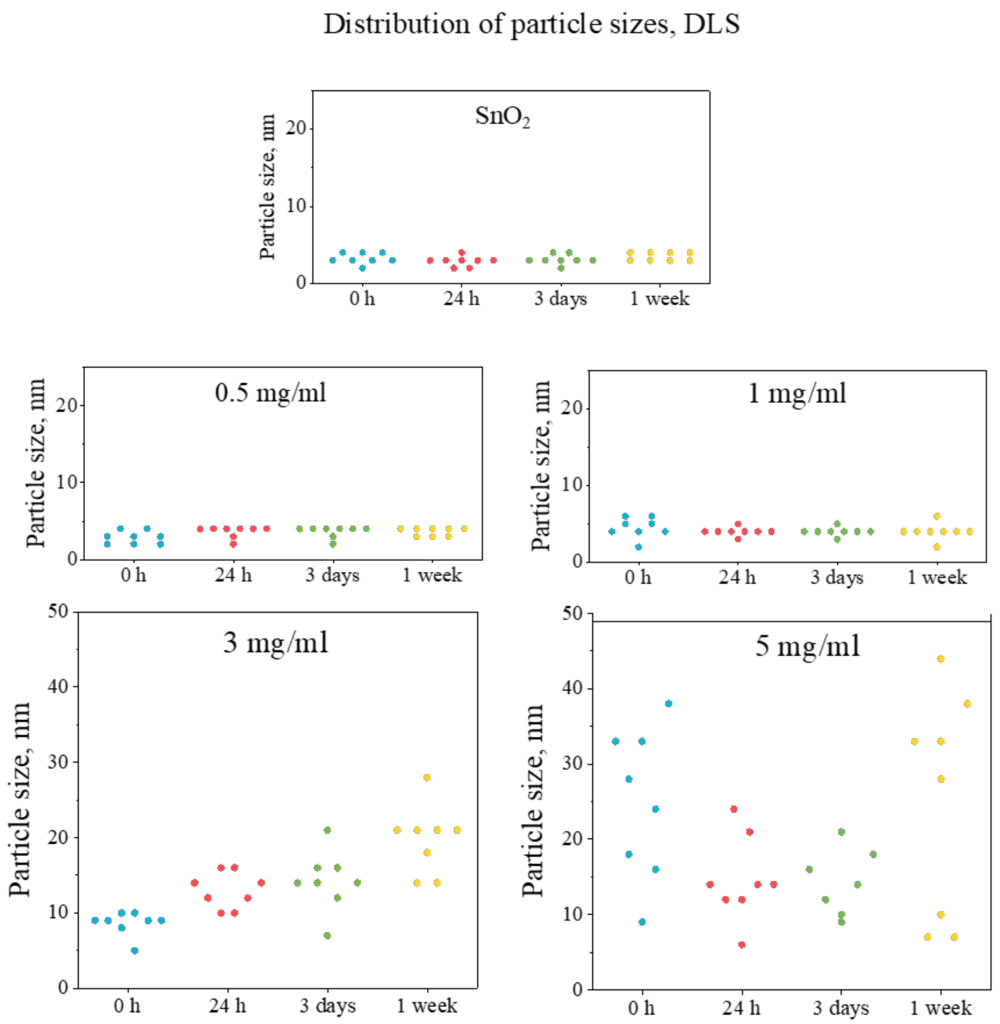

Figure 6.6: *Dynamic light scattering analysis of particle size in the* SnO_2 *solution with different concentrations of added ammonium salt over time.*

As can be seen in figure 6.6 the particle size in the SnO_2 solution as well as in the solutions with 0.5 mg/ml and 1 mg/ml salt are stable over time. However in the SnO_2 solution with 3 mg/ml additive the particle size increases over time. For the 5 mg/ml the particle size is significantly larger than for the other conditions already from the start, and the DLS analysis shows some varying results over time with the largest sizes encountered after 1 week. This implies that the particle size is already rather saturated at large sizes when the solution is made, and therefore appears rather random throughout the measurements.

The same trend as is seen in the DSL can be seen with the naked eye in terms of colour of the solutions. One important note when looking at figure 6.7 is that the vials in the two pictures are not the same, so the volume difference in the vials is not of consideration, and only the colour change is of importance.

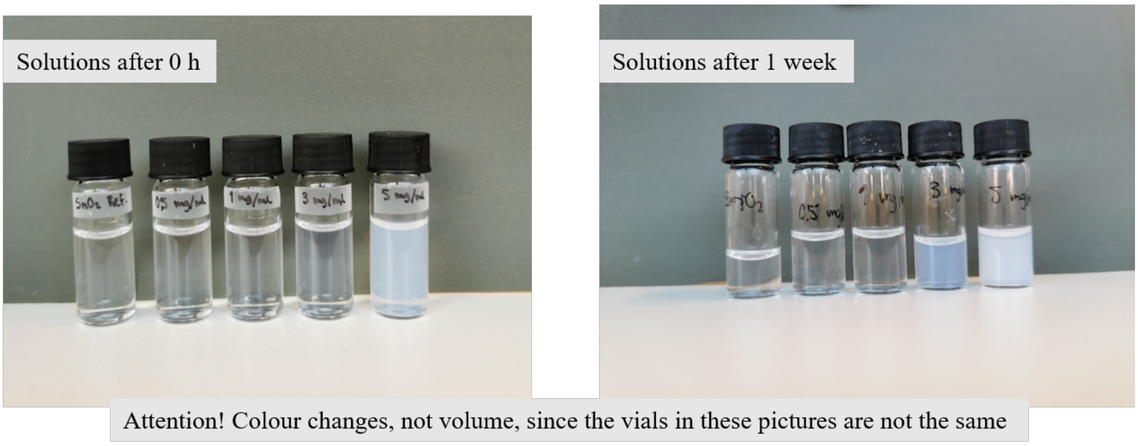

Figure 6.7: *Vials with different concentration of added salt over time. The colour change is due to chemical processes, the volume difference is due to the vials being different in the two pictures.*

The colour change in the vials with 3 mg/ml respective 5 mg/ml is clear and can be explained by the observations about the particle sizes made in the DLS measurement.

To further find an explanation for the differing particle sizes the pH of the solutions was measured at 0h. The result from the pH measurement can be seen in figure 6.8.

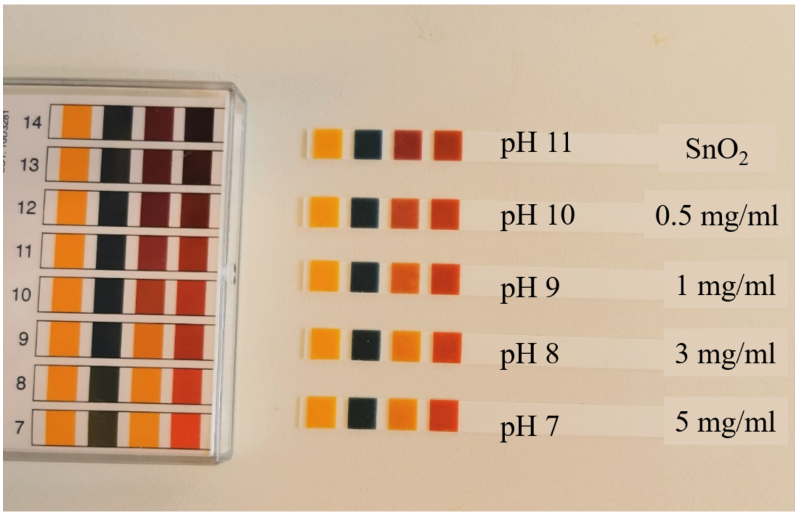

Figure 6.8: *A pH measurement with pH paper of the SnO_2 solutions with ammonium salt additive.*

From the pH measurement it is seen that the pH value decreases with an increased amount of ammonium salt in the solution. From the theory of the zeta potential this can explain the particle size in the solutions, such that the added salt influences the pH value, such that more added salt results on a lower pH. The pH in turn influences the zeta potential which influences the particle size in the solution. At a lower pH the particle size is expected to increase, which is what is observed in the DLS measurement.

It is of interest to investigate how the particle size affects the blocking properties of the SnO_2 film. Therefore cyclic voltammetry was performed on thin films of three different kinds:
1. Glass/FTO
2. Glass/FTO/SnO_2

3. Glass/FTO/SnO_2 with additive of different concentrations

The result can be seen in figure 6.9.

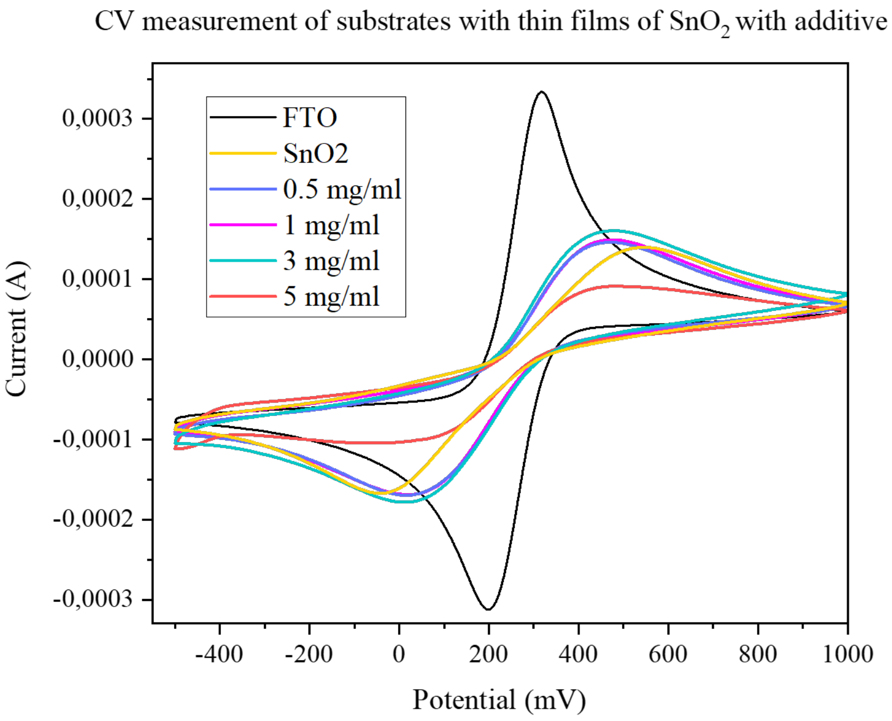

Figure 6.9: *Cyclic voltammetry measurement of thin films with the additive in the* SnO_2

From the CV measurement it is seen that the additive in the range 0.5 mg/ml - 3 mg/ml seem to have comparable blocking properties as the reference SnO_2 film. However, the film with 5 mg/ml additive has higher blocking properties, suggesting that its film is more compact than the others. The high blocking properties could cause less effective and slower electron transfer which might result in poorer cell performance. This could be part of the explanation why the SnO_2 film with 5 mg/ml yields lower PCE compared to the other concentrations. A clear difference is seen between the curve of the bare FTO and the SnO2-films, suggesting that the SnO2 film coverage is high.

To investigate the structure of the film, SEM was performed. From the SEM it was seen that the films were uniform and covered the surface well, as was expected from the CV measurement. Since the films looked similar only a few will be showed below in figure 6.10.

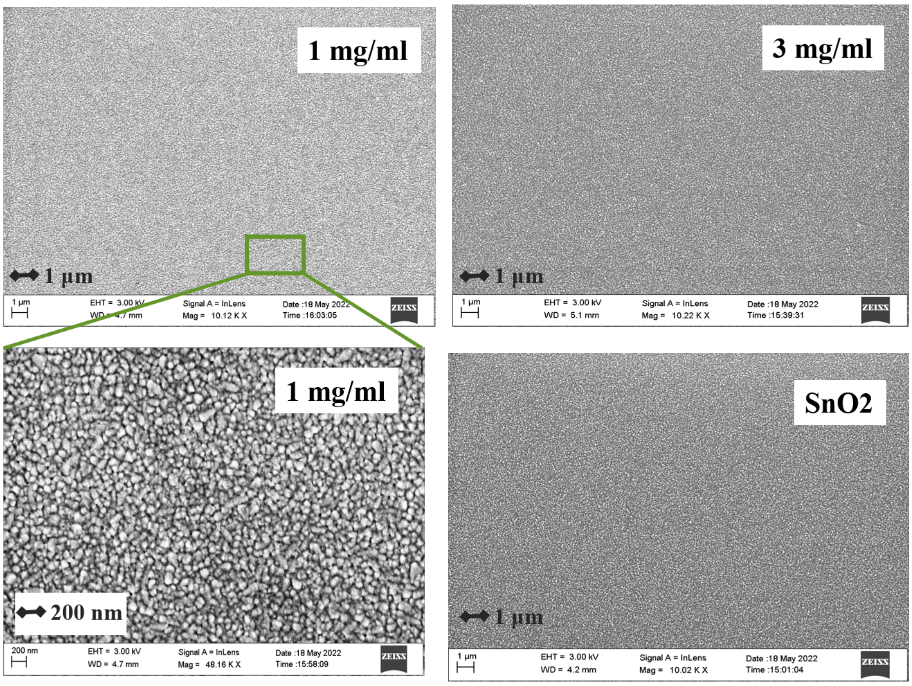

Figure 6.10: *SEM images of a selection of the films, representative for all of them. Bottom left is a zoom in in which it is seen that pin holes are not present.*

From the SEM images in figure 6.10 it is observed that the films are uniform and comparable to the SnO_2 film. From the zoomed in image in the bottom left corner it is also seen that there are no pinholes present in the film, and thus it covers the surface well.

To further investigate the surface of the films, AFM was performed to give an indication of the surface roughness. The result from the AFM is seen in figure 6.11.

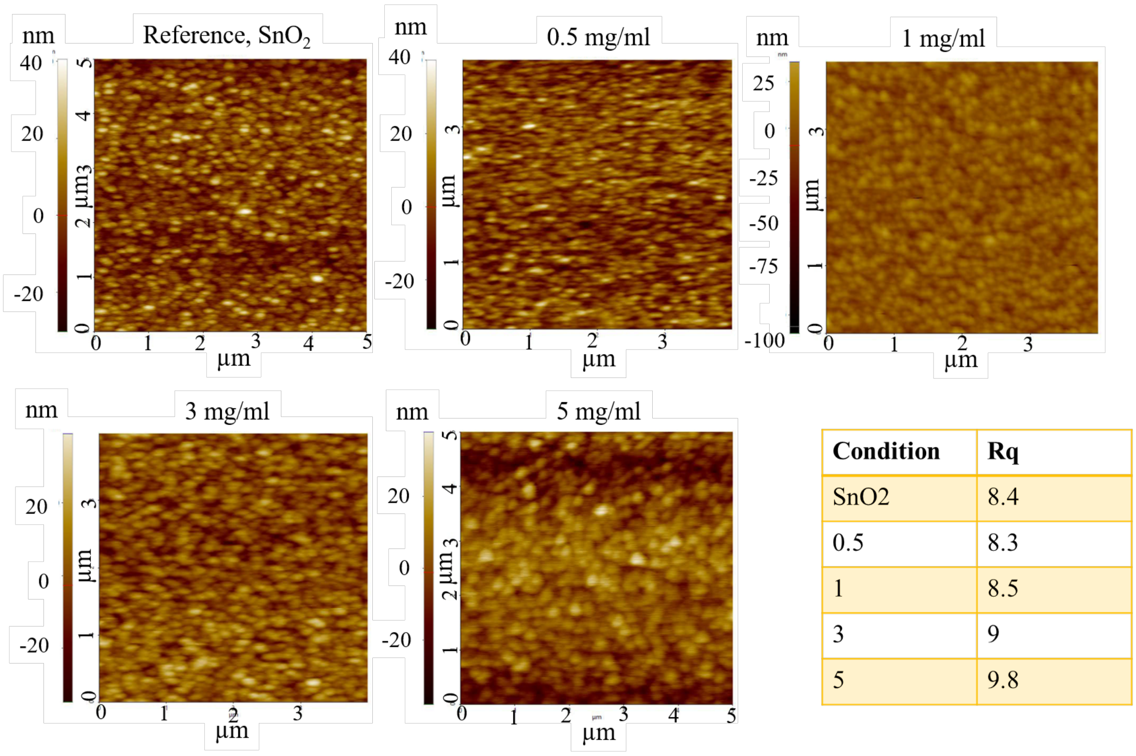

Condition	Rq
SnO2	8.4
0.5	8.3
1	8.5
3	9
5	9.8

Figure 6.11: *AFM of the films, with the scalebar illustrating the uniformity of the film, and the Rq value describing the surface roughness in the table in the bottom right corner.*

From the uniformity of the bar in the pictures from the AFM in figure 6.11 it is seen that the films are generally highly uniform, and cover the surface well, as was also observed with the SEM. Regarding the roughness it is seen from the Rq-value that the films with 0.5 mg/ml and 1 mg/ml additive have similar surface roughness as the SnO_2 film. The films with 3 mg/ml and 5 mg/ml additive show a slightly larger surface roughness. This is reasonable when thinking about the larger particle size of these two solutions.

It has been established that the films cover the surface well, and that the roughness increases with the concentration of additive in the solution, and that the highest concentration 5 mg/ml seems to yield higher blocking properties. The next step in the investigation is to see how the next layer, that is how the PSK film will behave on top of the SnO_2 with the additive. The first method to investigate this was through contact angle measurements. The result can be seen in figure 6.12.

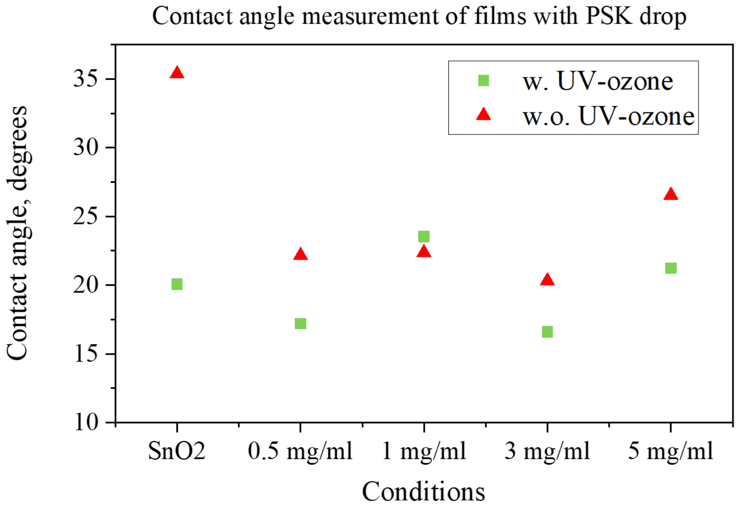

Figure 6.12: *Contact angle measurement of the films using perovskite solution*

From the contact angle measurement it is seen that the contact angle for the UV-ozone treated SnO_2 surfaces with bulk additive are comparable to the contact angle of the SnO_2, but there is no clear trend for the concentration of additive and the contact angle. However, the UV-ozone treatment does seem to improve the contact angle in all cases except for the sample with 1 mg/ml additive, where the two cases are similar. The take away from the contact angle measurement is that the PSK seems to spread equally well on the surfaces where the SnO_2 has been treated with the additive as for the pure SnO_2 surface. Also, since the UV-ozone treatment improved or did not affect the contact angle, it is good practice to do the UV-ozone treatment before depositing the PSK layer.

It is also of interest to take a look at the PSK layer itself. When the films were manufactured with the purpose of investigating the PSK layer, the humidity was already too high to achieve high quality PSK films, therefore the films in figure 6.13 do have pinholes, and the structure is not optimal. However, for the purpose of comparing the PSK films deposited onto pure SnO_2 and onto SnO_2 with additive, the films can be used anyway.

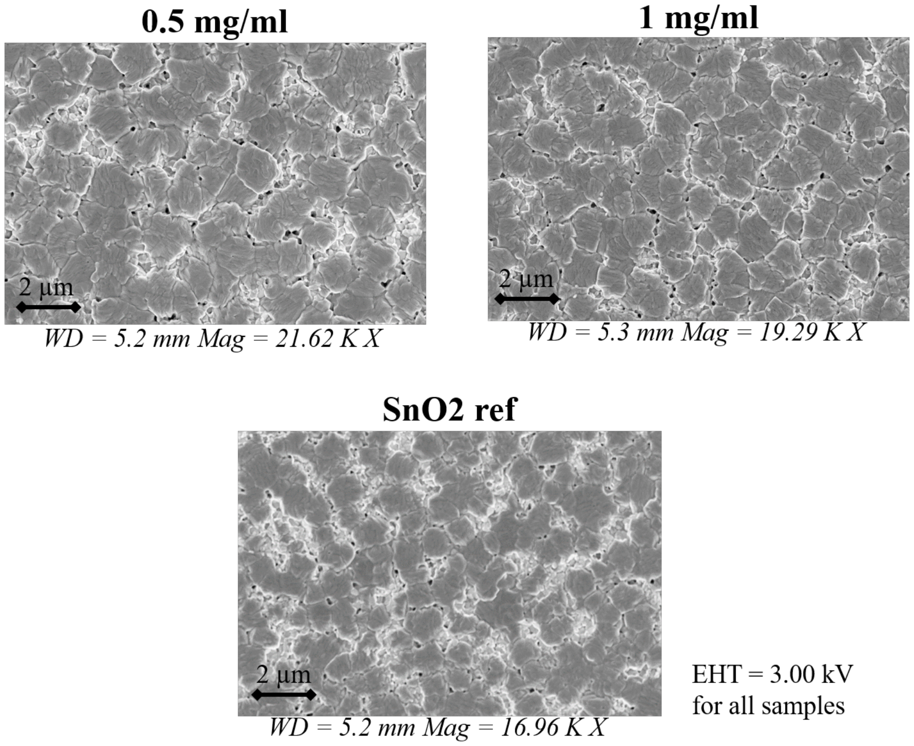

Figure 6.13: *SEM images of PSK deposited onto* SnO_2 *films.*

When looking at the PSK films in figure 6.13 it is seen that the structure of the PSK is similar on all substrates. It is therefore fair to say that the PSK structure does not seem to be affected by the additive in the SnO_2.

To further investigate the PSK film, an XRD measurement was performed on the films deposited onto the different substrates. The result can be seen in figure 6.14.

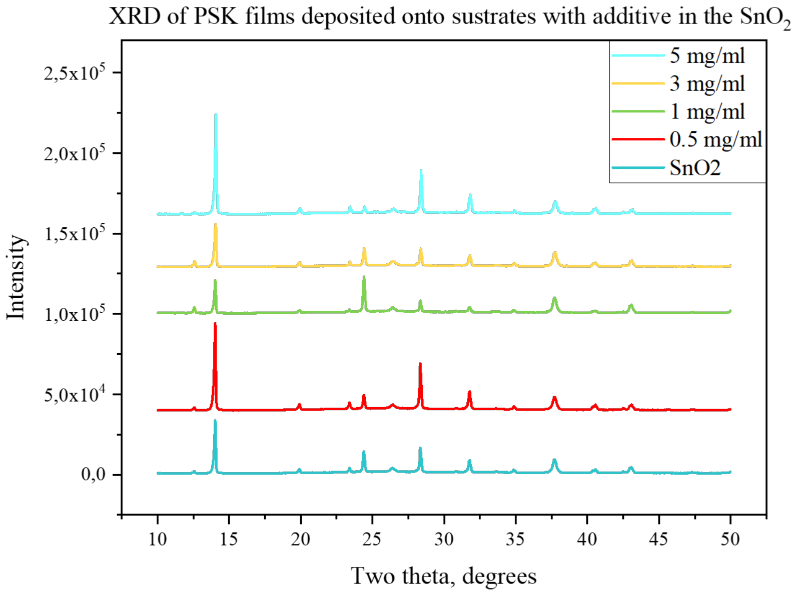

Figure 6.14: *XRD measurements of perovskite films deposited onto substrates with pure SnO_2 and SnO_2 films with different concentrations of the additive.*

As with the PSK manufactured for the SEM images, the PSK films for this measurement were manufactured in a environment with high humidity, and therefore the quality of the PSK film is not as good as for the SC manufactured at the beginning of the project. This is seen in figure 6.14 from the fact that the peaks differ somewhat in intensity from the different samples. However it is seen that the peaks appear at the same angles for all samples, suggesting that the PSK film on all samples is of comparable quality and thus the structure on the PSK is similar. This result therefore agrees with what was seen in the SEM measurement. What these results imply is that the top of the PSK film does not seem affected by the modification of the SnO_2 layer.

Since the structure of the PSK does not seem to be affected, it is of interest to investigate if other properties of the PSK have been affected. Therefore a PL measurement was performed and the result is seen in figure 6.15.

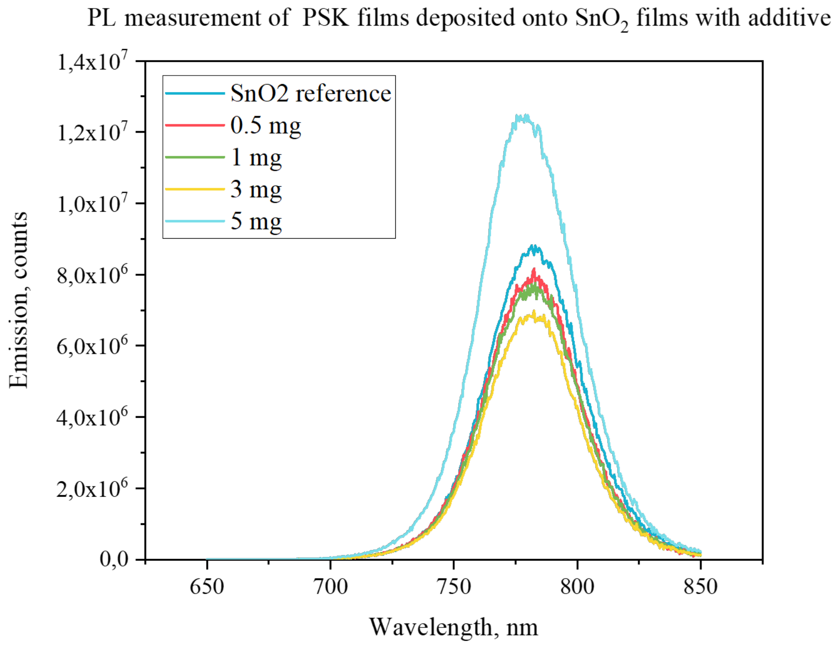

Figure 6.15: *PL measurement of perovskite films deposited onto SnO_2 thin films with and without additive.*

From the PL measurement in figure 6.15 it is seen that the PSK deposited onto SnO_2 with 5 mg/ml additive has the highest emission, followed by the reference film as second highest and then 0.5 mg/ml, 1 mg/ml and 3 mg/ml. This suggests that the films with 0.5 mg/ml – 1 mg/ml have a higher quenching than the reference, which means that the additive in this range facilitates the extraction of electrons from the PSK. The enhancement of the SnO_2 film with 5 mg/ml is not straight forward to interpret, and further investigations of the films such as the carrier mobility in the SnO_2 film, and the thickness of the PSK is needed.

From the results that are presented in this chapter it is at first seen from the CV measurement that the SnO_2 film with 5 mg/ml additive seems to have the highest blocking properties which could cause less effective electron transfer. This agrees with the PL results, where no quenching is observed.

From the SEM and AFM it is seen that the SnO_2 films with additive cover the surface well with high uniformity and without pinholes. This indicates that the films should work well as an ETL layer, which is also suggested from the high PCE results. One difference between the films is seen in the AFM result, where the films with higher concentration show higher roughness. This result is in line with what is expected since the particle size is larger for the solutions with higher concentration. It is therefore of interest to see if this roughness could be the cause of the lower performance of the cells with 5 mg/ml additive in the SnO_2. However, from the contact angle measurement and the SEM images of the PSK film, it seems like the structure and spreading of the PSK on top of the films is not affected by the different roughness. This is also confirmed from the XRD measurement where it is seen that the PSK films are similar.

The fact that the structure at the top of the PSK film does not seem to be affected by the alternation of the underlying layer is in this case a positive result, since the PSK deposited on pure SnO_2 generally has high quality. For this reason the goal would be to achieve the same high PSK quality as when pure SnO_2 is used, or if possible even higher quality. To get a even better understanding of the quality of the PSK film on the different ETL conditions, it would be preferred to manufacture PSK films in a low humidity environment to have crystals of higher quality. The PSK films in figure 6.13 are of poor quality and a high quantity of pinholes can be observed. This is due to high humidity when the films were manufactured. With high quality PSK films it could be demonstrated with higher precision if the quality is affected or not. Another measurement that could give an indication of the PSK structure is to investigate the PSK structure at the ETL/PSK interface.

One possible method to investigate the PSK structure at the ETL/PSK interface is to use epoxy tape to peel off the PSK layer. Then the structure of the PSK film that was in contact with the ETL can be examined to see if it is affected by the roughness of the SnO_2 film. It is also possible to image the cross section of the layers with SEM to see what the layers look like at the interfaces. That could also give an indication of the quality of the PSK when deposited on surfaces with different roughness.

However, from the initial results seen here on the PSK film it is more likely that the enhanced PCE is due to some property change of the SnO_2 film, since the PSK film itself seems to be unaffected. This is indeed seen from the PL measurement, where a change in the quenching properties is observed. The higher quenching of the films with concentrations 0.5-3 mg/ml of additive suggests a higher extraction of electrons from the PSK to the ETL, which could help explain the higher PCE observed for these films. However, since the structure of the films seemed equal, except for the roughness, it is likely that the higher quenching capacity originates from another property change of the SnO_2 that is not observed through the analysis performed here.

One possible change that could be relevant is the bandgap energy of the SnO_2 film. It is possible that the bandgap changes with the additive, and thereby facilitates the transport of electrons and blocks the holes even better than the pure SnO_2. To investigate if this is the case the bandgap energy should be measured. UV-vis absorption spectroscopy could be used to measure absorbance and reflectance, and in combination with knowledge about the thickness of the film from an intersection picture of the structure with SEM the bandgap can be calculated.

When compared to previous work in the field with ammonium salts, it is seen that ammonium salts have been used with great success for interface engineering for the PSK/HTL interface, with cells reaching efficiencies around 23% [22]. For the ETL/PSK interface however, not as much research with ammonium salts has been done. One study performed by Zheng et al. where an ammonium salt similar to the one used in this study was investigated as a pre-buried additive in the SnO_2 layer, reached a highest efficiency of 22.37% [45]. Another recent study by Che et al. investigate an ammonium chloride salt added in the bulk of the SnO_2 layer, as done in this study, and reach a highest efficiency of 22.27% [76]. Compared to these two reported findings, the modification of the SnO_2 layer presented in this project seems promising, as even higher efficiencies then reported elsewhere are reached.

As cannot be emphasised enough, the results presented in this study are highly preliminary due to the scarce amount of cells manufactured. To verify the results and their reproducibility the experiments conducted should be repeated with cells and films of high quality. It is of interest to continue with the manufacturing of cells in ambient conditions to investigate how this approach affects the efficiency of the cells. But it can also be of interest to compare cells manufactured in ambient condition, with cells manufactured in a glovebox to compare the outcome. Either way it is of big interest to continue the investigations and produce more cells with interface engineering using the ammonium salt.

7 Conclusion and outlook

In conclusion, it is seen that the UV-ozone treatment of the SnO_2 film has a noticeable impact on the performance of the PSC. Furthermore, the interfacial treatment of the SnO_2 layer with the ammonium salt does not seem to improve the efficiency of the cells when applied as an interfacial layer. However, when the ammonium salt is added to the bulk of the SnO_2, the preliminary results of the PCE indicate that the properties of the SnO_2 improve and lead to higher efficiency PSCs. The characterisation methods presented here do not give a full answer to what properties of the SnO_2 cause this positive change. Some indications are however given from the PL measurement and the CV, which indicate the salt in concentrations of 0.5-3 mg/ml improve the electron extraction from the PSK, and that the salt in a concentration of 5 mg/ml causes higher blocking of electrons in the SnO_2 film.

To verify reproducibility and statistical certainty of the results presented in this thesis, it is suggested to repeat the experiments and prepare more cells with the same concentrations of ammonium salt in the SnO_2 bulk. This is of importance since the number of cells produced with the ammonium salt added in the bulk of the SnO_2 in this study can only give an indication of how high efficiencies could be achieved by this interface engineering approach.

To further understand what leads to the observed improvement of the efficiencies, further investigations are needed. These investigations should focus on characterising more properties of the SnO_2 film, such as band gap and carrier mobility. It is also of interest to understand how the ammonium salt interacts with the SnO_2, and what properties of the salt are beneficial and cause this interaction.

Bibliography

[1] L. Al-Ghussain, "Global warming: review on driving forces and mitigation," *Environmental Progress & Sustainable Energy*, vol. 38, no. 1, pp. 13–21, 2019. [Online]. Available: https://aiche.onlinelibrary.wiley.com/doi/abs/10.1002/ep.13041

[2] Y. Xu and G. Cui, "Influence of spectral characteristics of the earth's surface radiation on the greenhouse effect: Principles and mechanisms," *Atmospheric Environment*, vol. 244, p. 117908, 2021.

[3] F. Cappelli, V. Costantini, and D. Consoli, "The trap of climate change-induced "natural" disasters and inequality," *Global Environmental Change*, vol. 70, p. 102329, 2021.

[4] I. Khan, F. Hou, M. Irfan, A. Zakari, and H. P. Le, "Does energy trilemma a driver of economic growth? the roles of energy use, population growth, and financial development," *Renewable and Sustainable Energy Reviews*, vol. 146, p. 111157, 2021.

[5] I. E. Agency, "Electricuty market report - jan 2022," 2022. [Online]. Available: https://www.iea.org/reports/electricity-market-report-january-2022

[6] ——, "World energy investment 2022," 2022. [Online]. Available: https://www.iea.org/reports/electricity-market-report-january-2022

[7] E. Commission, "Repowereu: A plan to rapidly reduce dependence on russian fossil fuels and fast forward the green transition*." [Online]. Available: https://ec.europa.eu/commission/presscorner/detail/en/IP_22_3131

[8] U. N. D. Programme. The sdgs in action. [Online]. Available: https://www.undp.org/sustainable-development-goals

[9] U. Nations. The paris agreement. [Online]. Available: https://www.un.org/en/climatechange/paris-agreement

[10] S. R. Sinsel, R. L. Riemke, and V. H. Hoffmann, "Challenges and solution technologies for the integration of variable renewable energy sources—a review," *Renewable Energy*, vol. 145, pp. 2271–2285, 2020. [Online]. Available: https://www.sciencedirect.com/science/article/pii/S0960148119309875

[11] V. Sivaram, *Taming the sun: Innovations to harness solar energy and power the planet*. MIT Press, 2018.

[12] M. Victoria, N. Haegel, I. M. Peters, R. Sinton, A. Jäger-Waldau, C. del Cañizo, C. Breyer, M. Stocks, A. Blakers, I. Kaizuka *et al.*, "Solar photovoltaics is ready to power a sustainable future," *Joule*, vol. 5, no. 5, pp. 1041–1056, 2021.

[13] G. C. Righini and F. Enrichi, "Solar cells' evolution and perspectives: a short review," *Solar Cells and Light Management*, pp. 1–32, 2020.

[14] W. Shockley and H. J. Queisser, "Detailed balance limit of efficiency of p-n junction solar cells," *Journal of applied physics*, vol. 32, no. 3, pp. 510–519, 1961.

[15] N. National Renewable Energy Laboratory, "Best research-cell efficiency chart." [Online]. Available: https://www.nrel.gov/pv/cell-efficiency.html

[16] P. Roy, N. K. Sinha, S. Tiwari, and A. Khare, "A review on perovskite solar cells: Evolution of architecture, fabrication techniques, commercialization issues and status," *Solar Energy*, vol. 198, pp. 665–688, 2020. [Online]. Available: https://www.sciencedirect.com/science/article/pii/S0038092X20300888

[17] R. A. Marques Lameirinhas, J. P. N. Torres, and J. P. de Melo Cunha, "A photovoltaic technology review: History, fundamentals and applications," *Energies*, vol. 15, no. 5, p. 1823, 2022.

[18] T. Ibn-Mohammed, S. Koh, I. Reaney, A. Acquaye, G. Schileo, K. Mustapha, and R. Greenough, "Perovskite solar cells: An integrated hybrid lifecycle assessment and review in comparison with other photovoltaic technologies," *Renewable and Sustainable Energy Reviews*, vol. 80, pp. 1321–1344, 2017. [Online]. Available: https://www.sciencedirect.com/science/article/pii/S1364032117307311

[19] A. A. Petrov, E. A. Goodilin, A. B. Tarasov, V. A. Lazarenko, P. V. Dorovatovskii, and V. N. Khrustalev, "Formamidinium iodide: crystal structure and phase transitions," *Acta Crystallographica Section E: Crystallographic Communications*, vol. 73, no. 4, pp. 569–572, 2017. [Online]. Available: https://www.ncbi.nlm.nih.gov/pmc/articles/PMC5382624/

[20] N. Marinova, S. Valero, and J. L. Delgado, "Organic and perovskite solar cells: Working principles, materials and interfaces," *Journal of colloid and interface science*, vol. 488, pp. 373–389, 2017.

[21] B. Dahal and W. Li, "Configuration of methylammonium lead iodide perovskite solar cell and its effect on the device's performance: A review," *Advanced Materials Interfaces*, p. 2200042, 2022.

[22] Y. Li, H. Xie, E. L. Lim, A. Hagfeldt, and D. Bi, "Recent progress of critical interface engineering for highly efficient and stable perovskite solar cells," *Advanced Energy Materials*, vol. 12, no. 5, p. 2102730, 2022.

[23] W. Yu, X. Sun, M. Xiao, T. Hou, X. Liu, B. Zheng, H. Yu, M. Zhang, Y. Huang, and X. Hao, "Recent advances on interface engineering of perovskite solar cells," *Nano Research*, vol. 15, no. 1, pp. 85–103, 2022.

[24] T. Leijtens, G. E. Eperon, N. K. Noel, S. N. Habisreutinger, A. Petrozza, and H. J. Snaith, "Stability of metal halide perovskite solar cells," *Advanced Energy Materials*, vol. 5, no. 20, p. 1500963, 2015.

[25] L. Contreras-Bernal, A. Riquelme, J. J. Gallardo, J. Navas, J. Idigoras, and J. A. Anta, "Dealing with climate parameters in the fabrication of perovskite solar cells under ambient conditions," *ACS Sustainable Chemistry & Engineering*, vol. 8, no. 18, pp. 7132–7138, 2020.

[26] C. Aranda, C. Cristobal, L. Shooshtari, C. Li, S. Huettner, and A. Guerrero, "Formation criteria of high efficiency perovskite solar cells under ambient conditions," *Sustainable Energy & Fuels*, vol. 1, no. 3, pp. 540–547, 2017.

[27] T. Kirchartz and U. Rau, "What makes a good solar cell?" *Advanced energy materials*, vol. 8, no. 28, p. 1703385, 2018.

[28] NREL, "Solar spectral irradiance: Air mass 1.5." [Online]. Available: https://www.nrel.gov/grid/solar-resource/spectra-am1.5.html

[29] H. Michaels, “A molecular guide to efficient charge transport: Coordination materials for photovoltaic cells,” Ph.D. dissertation, Acta Universitatis Upsaliensis, 2022.

[30] D. Lan, “The physics of ion migration in perovskite solar cells: Insights into hysteresis, device performance, and characterization,” *Progress in Photovoltaics: Research and Applications*, vol. 28, no. 6, pp. 533–537, 2020.

[31] H. Zhang, K. Song, L. Zhu, and Q. Meng, “Back-interface regulation for carbon-based perovskite solar cells,” *Carbon*, vol. 168, pp. 372–391, 2020.

[32] X. Zhang, Z. Yu, D. Zhang, Q. Tai, and X.-Z. Zhao, “Recent progress of carbon-based inorganic perovskite solar cells: From efficiency to stability,” *Advanced Energy Materials*, p. 2201320, 2022.

[33] Q. Jiang, L. Zhang, H. Wang, X. Yang, J. Meng, H. Liu, Z. Yin, J. Wu, X. Zhang, and J. You, “Enhanced electron extraction using sno2 for high-efficiency planar-structure hc (nh2) 2pbi3-based perovskite solar cells,” *Nature Energy*, vol. 2, no. 1, pp. 1–7, 2016.

[34] S. Agarwal and P. R. Nair, “Pinhole induced efficiency variation in perovskite solar cells,” *Journal of Applied Physics*, vol. 122, no. 16, p. 163104, 2017.

[35] J. Shi, X. Xu, D. Li, and Q. Meng, “Interfaces in perovskite solar cells,” *Small*, vol. 11, no. 21, pp. 2472–2486, 2015.

[36] C. M. Wolff, P. Caprioglio, M. Stolterfoht, and D. Neher, “Nonradiative recombination in perovskite solar cells: the role of interfaces,” *Advanced Materials*, vol. 31, no. 52, p. 1902762, 2019.

[37] K. Valadi, S. Gharibi, R. Taheri-Ledari, S. Akin, A. Maleki, and A. E. Shalan, “Metal oxide electron transport materials for perovskite solar cells: a review,” *Environmental Chemistry Letters*, vol. 19, no. 3, pp. 2185–2207, 2021.

[38] J. Lian, B. Lu, F. Niu, P. Zeng, and X. Zhan, “Electron-transport materials in perovskite solar cells,” *Small Methods*, vol. 2, no. 10, p. 1800082, 2018.

[39] P. Chetri and A. Choudhury, “Investigation of optical properties of sno2 nanoparticles,” *Physica E: Low-dimensional Systems and Nanostructures*, vol. 47, pp. 257–263, 2013.

[40] J. J. Yoo, G. Seo, M. R. Chua, T. G. Park, Y. Lu, F. Rotermund, Y.-K. Kim, C. S. Moon, N. J. Jeon, J.-P. Correa-Baena *et al.*, “Efficient perovskite solar cells via improved carrier management,” *Nature*, vol. 590, no. 7847, pp. 587–593, 2021.

[41] L. Xie, Z. Cao, J. Wang, A. Wang, S. Wang, Y. Cui, Y. Xiang, X. Niu, F. Hao, and L. Ding, “Improving energy level alignment by adenine for efficient and stable perovskite solar cells,” *Nano Energy*, vol. 74, p. 104846, 2020.

[42] E. H. Jung, B. Chen, K. Bertens, M. Vafaie, S. Teale, A. Proppe, Y. Hou, T. Zhu, C. Zheng, and E. H. Sargent, “Bifunctional surface engineering on sno2 reduces energy loss in perovskite solar cells,” *ACS Energy Letters*, vol. 5, no. 9, pp. 2796–2801, 2020. [Online]. Available: https://pubs.acs.org/doi/abs/10.1021/acsenergylett.0c01566

[43] L. Xiong, Y. Guo, J. Wen, H. Liu, G. Yang, P. Qin, and G. Fang, “Review on the application of sno2 in perovskite solar cells,” *Advanced Functional Materials*, vol. 28, no. 35, p. 1802757, 2018.

[44] S. Park, D. W. Kim, and S. Y. Park, “Improved stability and efficiency of inverted perovskite solar cell by employing nickel oxide hole transporting material containing ammonium salt stabilizer,” *Advanced Functional Materials*, p. 2200437, 2022.

[45] Z. Zheng, F. Li, J. Gong, Y. Ma, J. Gu, X. Liu, S. Chen, and M. Liu, “Pre-buried additive for cross-layer modification in flexible perovskite solar cells with efficiency exceeding 22%,” *Advanced Materials*, p. 2109879, 2022.

[46] N.-G. Park and K. Zhu, “Scalable fabrication and coating methods for perovskite solar cells and solar modules,” *Nature Reviews Materials*, vol. 5, no. 5, pp. 333–350, 2020.

[47] N. Sahu, B. Parija, and S. Panigrahi, “Fundamental understanding and modeling of spin coating process: A review,” *Indian Journal of Physics*, vol. 83, no. 4, pp. 493–502, 2009.

[48] L. Azar, “Cavitation in ultrasonic cleaning and cell disruption,” *Controlled Environments February*, pp. 14–17, 2009.

[49] J. R. Vig, “Uv/ozone cleaning of surfaces,” *Journal of Vacuum Science & Technology A: Vacuum, Surfaces, and Films*, vol. 3, no. 3, pp. 1027–1034, 1985.

[50] A. Goetzberger and V. U. Hoffmann, *Photovoltaic solar energy generation.* Springer Science & Business Media, 2005, vol. 112.

[51] G. A. Nemnes, C. Besleaga, A. G. Tomulescu, A. Palici, L. Pintilie, A. Manolescu, and I. Pintilie, “How measurement protocols influence the dynamic jv characteristics of perovskite solar cells: Theory and experiment,” *Solar Energy*, vol. 173, pp. 976–983, 2018.

[52] M. A. Green, “Tracking solar cell conversion efficiency,” *Nature Reviews Physics*, vol. 2, no. 4, pp. 172–173, 2020.

[53] J. A. Christians, J. S. Manser, and P. V. Kamat, “Best practices in perovskite solar cell efficiency measurements. avoiding the error of making bad cells look good,” pp. 852–857, 2015.

[54] P. A. Hassan, S. Rana, and G. Verma, “Making sense of brownian motion: colloid characterization by dynamic light scattering,” *Langmuir*, vol. 31, no. 1, pp. 3–12, 2015.

[55] V. Uskoković, R. Odsinada, S. Djordjevic, and S. Habelitz, “Dynamic light scattering and zeta potential of colloidal mixtures of amelogenin and hydroxyapatite in calcium and phosphate rich ionic milieus,” *Archives of oral biology*, vol. 56, no. 6, pp. 521–532, 2011.

[56] K. Pate and P. Safier, “12 - chemical metrology methods for cmp quality,” in *Advances in Chemical Mechanical Planarization (CMP)*, S. Babu, Ed. Woodhead Publishing, 2016, pp. 299–325. [Online]. Available: https://www.sciencedirect.com/science/article/pii/B9780081001653000127

[57] G. Midekessa, K. Godakumara, J. Ord, J. Viil, F. Lattekivi, K. Dissanayake, S. Kopanchuk, A. Rinken, A. Andronowska, S. Bhattacharjee *et al.*, “Zeta potential of extracellular vesicles: toward understanding the attributes that determine colloidal stability,” *Acs Omega*, vol. 5, no. 27, pp. 16 701–16 710, 2020.

[58] J. F. Rusling and S. L. Suib, “Characterizing materials with cyclic voltammetry,” *Advanced Materials*, vol. 6, no. 12, pp. 922–930, 1994.

[59] N. Elgrishi, K. J. Rountree, B. D. McCarthy, E. S. Rountree, T. T. Eisenhart, and J. L. Dempsey, “A practical beginner’s guide to cyclic voltammetry,” *Journal of chemical education*, vol. 95, no. 2, pp. 197–206, 2018.

[60] K. Akhtar, S. A. Khan, S. B. Khan, and A. M. Asiri, "Scanning electron microscopy: Principle and applications in nanomaterials characterization," in *Handbook of materials characterization*. Springer, 2018, pp. 113–145.

[61] A. Alyamani and O. Lemine, "Fe-sem characterization of some nanomaterial," in *Scanning electron microscopy*. IntechOpen, 2012.

[62] H. Zhang, J. Huang, Y. Wang, R. Liu, X. Huai, J. Jiang, and C. Anfuso, "Atomic force microscopy for two-dimensional materials: A tutorial review," *Optics Communications*, vol. 406, pp. 3–17, 2018.

[63] D. Y. Abramovitch, S. B. Andersson, L. Y. Pao, and G. Schitter, "A tutorial on the mechanisms, dynamics, and control of atomic force microscopes," in *2007 American Control Conference*. IEEE, 2007, pp. 3488–3502.

[64] V. J. Bellitto and M. I. Melnik, "Predicting macroscale effects through nanoscale features," in *Atomic Force Microscopy-Imaging, Measuring and Manipulating Surfaces at the Atomic Scale*. IntechOpen, 2012.

[65] G. Lamour, A. Hamraoui, A. Buvailo, Y. Xing, S. Keuleyan, V. Prakash, A. Eftekhari-Bafrooei, and E. Borguet, "Contact angle measurements using a simplified experimental setup," *Journal of chemical education*, vol. 87, no. 12, pp. 1403–1407, 2010.

[66] A. Krishnan, Y.-H. Liu, P. Cha, R. Woodward, D. Allara, E. A. Vogler *et al.*, "An evaluation of methods for contact angle measurement," *Colloids and Surfaces B: Biointerfaces*, vol. 43, no. 2, pp. 95–98, 2005.

[67] Attension, *Influence of droplet volume on contact angle*, Biolin scientific, [Technology note] 6], 2016. [Online]. Available: https://cdn2.hubspot.net/hubfs/516902/Pdf/Attension/Tech%20Notes/AT-TN-06-Influence-drop-volume-contact-angle-160401.pdf?t=1516102020835

[68] J. Drelich, J. D. Miller, and J. Hupka, "The effect of drop size on contact angle over a wide range of drop volumes," *Journal of colloid and interface science*, vol. 155, no. 2, pp. 379–385, 1993.

[69] D. K. Unruh and T. Z. Forbes, "X-ray diffraction techniques," *Analytical geomicrobiology: a handbook of instrumental techniques (eds Alessi DS, Veeramani H, Kenney L)*, pp. 215–237, 2019.

[70] N. E. Widjonarko, "Introduction to advanced x-ray diffraction techniques for polymeric thin films," *Coatings*, vol. 6, no. 4, p. 54, 2016.

[71] M. Bouroushian, T. Kosanovic *et al.*, "Characterization of thin films by low incidence x-ray diffraction," *Cryst. Struct. Theory Appl*, vol. 1, no. 3, pp. 35–39, 2012.

[72] Y. Waseda, E. Matsubara, and K. Shinoda, *Diffraction from Polycrystalline Samples and Determination of Crystal Structure*. Berlin, Heidelberg: Springer Berlin Heidelberg, 2011, pp. 107–167. [Online]. Available: https://doi.org/10.1007/978-3-642-16635-8_4

[73] S. Perkowitz, *Optical characterization of semiconductors: infrared, Raman, and photoluminescence spectroscopy*. Elsevier, 2012.

[74] G. Baryshnikov, B. Minaev, and H. Ågren, "Theory and calculation of the phosphorescence phenomenon," *Chemical reviews*, vol. 117, no. 9, pp. 6500–6537, 2017.

[75] A. Erbe, S. Nayak, Y.-H. Chen, F. Niu, M. Pander, S. Tecklenburg, and C. Toparli, “How to probe structure, kinetics, and dynamics at complex interfaces in situ and operando by optical spectroscopy,” in *Encyclopedia of Interfacial Chemistry*, K. Wandelt, Ed. Oxford: Elsevier, 2018, pp. 199–219. [Online]. Available: https://www.sciencedirect.com/science/article/pii/B9780124095472140612

[76] Z. Che, L. Zhang, J. Shang, Q. Wang, Y. Zhou, Y. Zhou, and F. Liu, “Organic ammonium chloride salt incorporated sno2 electron transport layer for improving performance of perovskite solar cells,” *Sustainable Energy & Fuels*, 2022.